Apatite: A new redox proxy for silicic magmas?

A.J. Miles[a,*], C.M. Graham[a], C.J. Hawkesworth[b], M.R. Gillespie[c], R.W. Hinton[a], G.D. Bromiley[a] and EMMAC[d]

[a]*School of GeoSciences, King's Buildings, West Mains Road, University of Edinburgh Edinburgh, EH9 3JW, UK*

[b]*School of Geography and Geosciences, University of St Andrews, North Street, St Andrews, KY16 9AL, UK*

[c]*British Geological Survey, Murchison House, West Mains Road, Edinburgh, EH9 3LA, UK*

[d]*Edinburgh Materials and Micro-Analysis Centre, School of GeoSciences, King's Buildings, West Mains Road, University of Edinburgh, Edinburgh, EH9 3JW, UK*

**Current address: School of Geology, Geography and the Environment, Penrhyn Road, Kingston upon Thames, Surrey KT1 2EE. Email: Andrew.Miles@kingston.ac.uk Tel. +44 (0)20 8417 2492*

Abstract

The oxidation states of magmas provide valuable information about the release and speciation of volatile elements during volcanic eruptions, metallogenesis, source rock compositions, open system magmatic processes, tectonic settings and potentially titanium (Ti) activity in chemical systems used for Ti-dependent geothermometers and geobarometers. In this paper we explore the use of Mn in apatite as an oxybarometer in intermediate and silicic igneous rocks. Increased Mn concentrations in apatite in granitic rocks from the zoned Criffell

granitic pluton (southern Scotland) correlate with decreasing Fe_2O_3 (Fe^{3+}) and Mn in the whole-rock and likely reflect increased Mn^{2+}/Mn^{3+} and greater compatibility of Mn^{2+} relative to Mn^{3+} in apatite under reduced conditions. Fe^{3+}/Fe^{2+} ratios in biotites have previously been used to calculate oxygen fugacities (fO_2) in the outer zone granodiorites and inner zone granites where redox conditions have been shown to change from close to the magnetite-hematite buffer to close to the nickel-nickel oxide buffer respectively (Stephens et al., 1985). This trend is apparent in apatite Mn concentrations from a range of intermediate to silicic volcanic rocks that exhibit varying redox states and are shown to vary linearly and negatively with log fO_2, such that

$$\log fO_2 = -0.0022(\pm 0.0003)\ \mathrm{Mn\ (ppm)} - 9.75(\pm 0.46)$$

Variations in the Mn concentration of apatites appear to be largely independent of differences in the Mn concentration of the melt. Apatite Mn concentrations may therefore provide an independent oxybarometer that is amenable to experimental calibration, with major relevance to studies on detrital mineral suites, particularly those containing a record of early Earth redox conditions, and on the climatic impact of historic volcanic eruptions.

1. Introduction

Redox conditions play a pivotal role in determining the metallogenic properties of plutonic bodies (Ishihara, 1977, 1981; Belvin, 2004) and they control the molecular speciation of volcanic gases containing sulphur, carbon and hydrogen exsolved on eruption (e.g. Scaillet et al., 1998). These volatile gasses in turn control magma dynamics (e.g. Huppert and Woods, 2002; Gonnerman and Manga, 2003) and the composition and evolution of the Earth's

atmosphere (Kasting et al., 1993; Trail et al., 2011; Scaillet and Gaillard, 2011; Binder and Keppler, 2011). For example, sulphur is thought to partition preferentially into fluid phases relative to silicate melts under oxidising conditions, resulting in greater sulphur emissions from explosive eruptions of oxidised silicic magmas relative to eruptions of reduced magmas (Scaillett et al., 1998). The eruption of oxidised silicic magmas is therefore likely to have a significantly greater climatic impact (Robock, 2000) than those of reduced magmas. Furthermore, it is becoming increasingly apparent that redox conditions strongly influence titanium activity (a_{TiO2}) in chemical systems, to the extent that it has recently been suggested that redox state may be used as proxy for titanium activity (Ghiorso and Gualda, 2013). Constraining redox conditions may therefore be important for the successful application of a_{TiO2}-dependent geothermometers and geobarometers (Wark and Watson, 2006; Ferry and Watson, 2007; Hayden et al. 2008; Thomas et al. 2010; Ghiorso and Gualda, 2013).

Redox states of magmas and their variations reflect their sources and tectonic settings and also provide important constraints on their ascent and evolution (e.g. Ishihara, 2004). It is widely accepted that calc-alkaline magmas, found mainly around active subduction zones, are more oxidised than their tholeiitic counterparts (Gill, 1981; Arculus, 2003; Carmichael, 1991; Kelly and Cottrell, 2009; Lee et al., 2010). This is reflected in Fe depletion during differentiation of calc-alkaline magmas that results from the stabilisation of Fe^{3+}-bearing oxide minerals under more oxidising conditions (Gill, 1981).

Quantitative estimates of redox conditions are calculated using oxygen fugacity (fO_2) – a measure of the availability and capacity of oxygen to participate in reactions of minerals and fluids. The higher oxygen fugacities of calc-alkaline magmas may be inherited from source regions, develop through differentiation and assimilation (see Lee et al., 2010), or be

achieved by redox reactions during degassing (Holloway et al., 2004; Burgisser and Scaillet, 2007). Estimating the fO_2 conditions of magmas has traditionally relied on the measured Fe^{2+}/Fe^{3+} ratios of magmatic glasses and mineral phases (Carmichael and Ghiorso 1990). The effects of alteration can reduce the reliability of results, but they can to some extent be overcome by examining heterovalent transition elements such as V and Cr that are generally immobile during alteration, but whose partitioning is redox-sensitive (Canil, 1997).

Accessory minerals provide a particularly robust record of magma conditions, and their frequent preservation in the sedimentary record as detrital minerals means they can be used to document the formation and evolution of magmas now lost from the geological record. A method of constraining magma redox conditions from detrital minerals could provide an important new tool for examining Earth evolution processes. The concentrations of redox sensitive elements such as Fe, Mn, Ce and Eu in accessory minerals offer great potential in obtaining reliable estimates of redox conditions. For example Ce anomalies in zircon have recently been experimentally calibrated at varying fO_2 conditions by Trail et al., (2011) in order to estimate the oxidation state of Hadean magmas.

In this paper, we have evaluated the redox conditions in granitic rocks from the post-Caledonian Criffell pluton in southern Scotland using Ce anomalies in zircon and Fe^{3+}/Fe^{2+} ratios in biotite (Stephens et al., 1985). The former method is shown to result in large uncertainties in calculated fO_2 values. We investigate the use of Mn concentrations in coexisting apatites to record changing redox conditions in this pluton. We also examine the capacity of Mn concentrations in apatites to provide a reliable proxy for redox conditions in a range of volcanic rocks where independent estimates of redox conditions are available. Apatite Mn concentrations may permit robust estimates of redox conditions in a range of

magma compositions, and they have great potential for constraining redox conditions on the early Earth through application to detrital minerals. Reliable estimates of the redox conditions of historic volcanic eruptions may also enable better estimates of their climatic impact.

2. The Criffell pluton

The Criffell pluton is one of a large number of post-Caledonian granitic plutons in northern parts of the United Kingdom. The pluton was emplaced at ~ 410 Ma (Miles et al., 2013b) into low-grade wackes and pelites of Llandovery to Wenlock age in the Southern Uplands accretionary prism in southern Scotland (Fig. 1). The pluton is normally zoned (Stephens et al., 1980, 1985), with outer zones (1 and 2) of metaluminous granodiorite (~ 58 wt % SiO_2), a transition zone (3), and inner zones (4 and 5) of peraluminous granite (~ 72 wt % SiO_2). Granodiorite samples contain primary hornblende (with occasional cores of clinopyroxene), biotite, plagioclase, potassium feldspar, quartz and accessory sphene, zircon, apatite, allanite and magnetite. Granite samples contain primary muscovite and small amounts of monazite but lack hornblende, sphene and the abundant zircon and magnetite that characterise the granodiorites. The small amounts of magnetite in the most silicic zone containing zircon (Zone 4) show evidence of trellis oxidation-exsolution (Fig. 2). This is thought to reflect exsolution of magnetite and ulvospinel, with subsequent oxidation of ulvospinel to ilmenite (Haggerty, 1991).

A general trend of decreasing Fe_2O_3 (Fe^{3+}) with indices of differentiation (e.g. SiO_2) in the whole-rock suite is supported by independent estimates of oxygen fugacity from Fe compositions in biotite (Stephens et al., 1985). This trend has been attributed to a gradual

transition from more oxidising conditions in outer zones (close to the hematite-magnetite buffer) to less oxidising conditions in the inner zones (close to the nickel-nickel oxide (NNO) buffer). The assemblage quartz + magnetite + sphene also indicates conditions more oxidising than the NNO buffer + 2 log units of oxygen fugacity (Dilles, 1987; Wones 1989; Strack and Dilles, 1998) in the outer zone of the Criffell pluton. Furthermore, a gradual decrease in the modal abundance of magnetite and sphene in more silicic zones of the Criffell pluton indicate that these magmas are more reduced (Xirouchakis et al., 2001). Whole-rock isotope modelling suggests that the most reduced zones contain up to ~ 30% of assimilated reduced sedimentary rocks, consistent with their peraluminous compositions (Stephens et al., 1985; Miles et al., 2013a).

Apatite crystals up to 1mm long are found in all zones of the pluton, typically occurring as inclusions in most major rock-forming minerals including zircon. Apatite REE compositions have been shown to reflect bulk compositional changes in the magma and appear to have crystallised over extended periods of magma evolution relative to other phases (Miles et al., 2013a). Zircon occurs in all zones, although only in small amounts in Zone 5 (innermost and most silicic granite). The small number of zircon crystals found in Zone 5 are often highly fractured, possibly due to radiation damage. Zircon U-Pb ages (Miles et al., 2013b) reveal no inherited zircon in any part of the pluton, consistent with the conclusions of an earlier study (Pidgeon and Aftalion, 1978). The general absence of resorption surfaces within concentrically zoned zircon crystals suggests that most are primary and do not represent antecrysts.

3. Methodology

Whole-rock major oxide compositions were determined by Stephens and Halliday (1980) using 'rapid wet' methods and the two-solution method of Riley (1958). SiO_2 and Al_2O_3 were analysed by spectrophotometric methods; Na_2O and K_2O by atomic emission; total FeO, MnO, MgO and CaO by atomic absorption; TiO_2 and P_2O_5 by colorimetry; and ferrous iron by titration with potassium dichromate.

Apatites from the outer four zones of the Criffell pluton were analysed in thin section to provide textural context. Zircon-hosted apatite inclusions were analysed following standard heavy liquid and magnetic separation of zircon and mounting in epoxy blocks. Mn abundances were measured using a Cameca SX-100 electron microprobe at the University of Edinburgh (concentrations converted from weight % to ppm are in Table 1). Wavelength dispersive (WDS) analyses were carried out using PC0, LTAP, LPET and LIF dispersion crystals. A ~1 μm, 20 kV beam, initially at 10 nA and defocused (to minimise the loss of alkali elements during analysis) and subsequently at 60 nA was used for analysing trace and most major elements.

Apatite REE concentrations were determined using a Cameca ims4f ion microprobe at the University of Edinburgh, with a 5 nA $^{16}O^-$ primary ion beam at 15 keV net impact energy and a spot size of approximately 15 μm. Only high energy secondary ions (100-140 eV) were measured in order to reduce molecular ion overlap. F^-/Ca^{2+} ion yields were determined using Durango and Wilberforce standards. Corrections were made for CeF at mass 159 based on the observed F content and previous measurements of 159 variability with energy measured on Durango apatite. The LREE ion yields were calculated relative to glass standard SRM610 (Pearce et al., 1997) and multiple apatite standards (Steven Burgman, pers. comm.), but because of limited element coverage, the HREE were based on measurements of Durango

apatite alone. Uncertainties in absolute concentrations should be better than 20% but relative concentrations are <5% where not limited by counting statistics. Analysis spots were subsequently examined for cracks and inclusions using back-scattered electron (BSE) and cathodoluminescence (CL) images of polished surfaces obtained with a Philips XL30P Scanning Electron Microscope (SEM) at the University of Edinburgh.

Approximately 100 zircon crystals per sample were separated, with ~ 10 crystals per sample analysed by ion microprobe at the University of Edinburgh using a Cameca ims-4f ion microprobe. Zircon trace elements were analysed at 15 keV net impact energy using a ~ 15 μm diameter primary $^{16}O^-$ beam at ~5 nA with 4.5 keV secondary positive ions measured at ~ 120 keV offset following the method of Hinton and Upton (1991). Measurements were made at low mass resolution applying a large energy offset (100-140 eV) to minimise molecular ion overlaps. Corrections were made for $ZrSiO^+$ based on the mass 134 count rates and were typically equivalent to 0.015 ppm La and 0.002 ppm Pr. Analysis times were set longer for species at lower concentrations or for low abundance isotopes giving relatively constant errors across the LREE (with the exception of Ce). For a typical zircon pattern increasing in concentration from 0.05 ppm La to 0.2 ppm Eu, the counting errors of a single analysis for all the LREE is approximately 30% (1 SD). This error falls to 8% if the concentrations are 10 times higher (i.e. values typical for the measurements made here). For Ti (used for thermometry), 1SD errors are typically 5% at 8ppm, rising to 10% at 2.5 ppm and about 7% in the normal 4-5 ppm range. The detector background was measured at mass 130.5 and was <0.01 cps (equivalent to ≈0.005 ppm La) based on a combined measurement over 2 days and no corrections were made for detector background. Corrections were made for the overlap of LREE oxides on HREE. Because of the low LREE abundances, corrections for LREE oxides on the HREE were rarely more than 3% and any error related to the correction likely to be

significantly less than 1%. Concentrations were determined relative to NIST610 glass (Pearce et al., 1997) in the similar manner to that described in Weidenbeck et al. (2004) and Hinton and Upton (1991) and secondary zircon standard 91500 was used (Weidenbeck et al. (2004).

4 Results

4.1 Mn, Fe and Eu contents in apatites and whole-rocks

All zones of the Criffell pluton contain predominantly fluor-apatite ($Ca_5(PO_4)_3$)F. Total Mn concentrations in apatite increase systematically by up to a factor of ~ 27 between Zone 1 (190 – 582 ppm) and Zone 4 (1713 - 5076 ppm) (Fig. 3a; Table 1). Yet Mn in the whole-rock shows a subtle decrease with increasing SiO_2 (Fig. 3a; Supplementary Material 1), demonstrating that Mn is more easily partitioned into apatite in the more silicic zones. Electron probe traverses carried out across individual crystals in zones 1 and 2 reveal no significant compositional zonation, with almost all Mn analyses within analytical error (~150ppm) of each other (Supplementary Material 2). There is no evidence to suggest that the Mn concentrations of apatite inclusions are dependent on the host mineral (Table 1). Total Fe concentrations in apatites are mainly between ~ 100 and 4600 ppm and when not distinguished according to their host phase, appear not to vary systematically between zones and display similar degrees of variability within and between zones (Fig. 3b). However, unlike Mn, Fe concentrations in all zones show marked increases in apatites hosted by Fe-rich minerals such as hornblende and biotite. This is likely to reflect secondary fluorescence of Fe caused by the proximity of analytical spots in apatite inclusions to Fe-rich host minerals. Using a beam voltage of 20 kV, penetration depths are likely to be ~ 9µm (calculated using Electron Flight Simulator version 3.01). However, the range of

220 characteristic X-rays and Bremsstrahlung that are generated by incident electrons is typically
221 one or two-orders-of-magnitude greater (up to several tens or hundreds of microns, Llovet
222 and Galan, 2003). Fe concentrations in apatites hosted by Fe-poor minerals such as zircon,
223 quartz and feldspar display the same trend shown by Mn, increasing from between ~ 100 and
224 300 ppm in zones 1 and 2,140 and 840 ppm in Zone 3 and 260 and 1700 ppm in Zone 4 (Fig.
225 3b). Whole-rock Fe_2O_3 (Fe^{3+}) varies from ~2.1×10^3 ppm to 1.8×10^4 ppm and shows a general
226 decrease with increasing SiO_2 (Fig. 3b). Mn/Fe ratios in apatites (excluding those hosted in
227 hornblende and biotite) show an increase in their maximum values from Zone 1 (all < 3) to
228 Zone 4 (all < 12) (Fig. 3c). For whole-rock, MnO/FeO_{Total} (where 'Total' refers to Fe_2O_3 +
229 FeO) increases from 0.017 to 0.035 with increasing SiO_2 (Fig. 3c).
230
231 Chondrite-normalised REE profiles for the Criffell apatites show a marked increase in the
232 magnitude of their negative Eu anomalies (Eu/Eu*) from zones 1 to 4 (Miles et al., 2013a)
233 and are presented here in Figure 4. Apatites in Zone 1 generally have Eu/Eu* values of
234 between 0.7 and 1, while those from zones 4 and 5 have Eu/Eu* values that are all <0.4 (Fig.
235 4). Whole-rock compositions from the Criffell pluton are noteworthy for their very small Eu
236 anomalies, particularly in the granodiorite zones (Stephens et al., 1985), suggesting that
237 apatites cannot have inherited their Eu anomaly characteristics from the bulk-rock magmas.

238 *4.2 Ce in zircon and crystallisation temperatures*

239
240 Positive Ce anomalies (calculated using the expression $Ce/Ce^* = Ce_N/(La_N \times Pr_N)^{1/2}$, where
241 element abundances are normalised (N) to chondrite, are a common feature of igneous zircon
242 (Fig. 5; Table 2), reflecting the ability of Ce to exist as Ce^{4+} under oxidising conditions
243 (Hinton and Upton, 1991; Ballard et al., 2002; Hoskin and Schaltegger, 2003; Trail et al.,

2011; 2012; Burnham and Berry, 2012). At magmatic temperatures, homogenisation of REE concentrations at a 10 μm scale in zircon only occurs on timescales greater than the age of the Earth (Cherniak and Watson, 2003). Unlike Eu anomalies, Ce anomalies are not influenced by feldspar crystallisation. Large Ce anomalies in zircon are thought to reflect a ~ 4 to 6 orders of magnitude increase in the compatibility of Ce^{4+} relative to Ce^{3+} (the latter represents 99.0% to 99.7% of the total Ce in most melts) rather than large increases in the abundance of Ce^{4+} (Ballard et al., 2002; Colombini et al., 2011). The increased solubility of Ce^{4+} is likely to result from similarities in its size and charge relative to Zr^{4+} for which it substitutes. Median Ce/Ce* values for zircon in zones 1 to 3 of the Criffell pluton are similar and range from 52 to 63 (Fig. 5b), while the median value for Zone 4 is much lower at 28. Every zone is characterised by significant scatter in Ce/Ce* values, the three outermost zones having interquartile values (within which 50 % of the data reside) of ~ 18 to 34 while the innermost analysed zone (Zone 4) has an interquartile value of ~ 107.

Zircon crystallisation temperatures have been calculated (Table 2) using the modified Ti-in-zircon thermometer of Ferry and Watson (2007), allowing for variations in the activity of Si and Ti. The inherent problems of assessing these activities at the time of zircon crystallisation mean that the thermometer provides only semi-quantitative estimates of crystallisation temperatures. However, overestimates or underestimates of silica and titanium activities result in offsetting errors in crystallisation temperatures (Ferry and Watson, 2007). The abundance of quartz in all zones makes it likely that silica activity was at or close to unity during zircon saturation, so estimated crystallisation temperatures will be towards the top of the range. A lack of rutile in analysed samples indicates that titanium activity was below unity; however, the presence of other Ti-rich phases such as sphene in the outer zones of the pluton indicates that Ti activity was not very low (an observation made in other plutons, e.g.

Hayden and Watson, 2007; Claiborne et al., 2010). We therefore assume a titanium activity value of 0.7 after Claiborne et al., (2010). Average zircon crystallisation temperatures and standard deviations are effectively indistinguishable at 680 (± 32) ^{o}C, 669 (± 24) ^{o}C, 681 (± 38) ^{o}C and 634 (± 32) ^{o}C in zones 1 to 4 respectively (Table 2).

5. Discussion

Mn concentrations increase significantly in apatite relative to whole-rock during magma evolution in a number of granitic plutons (SiO_2 > 63wt%) that exhibit evidence for assimilation of sedimentary rocks (Fig. 6) (Sha and Chappell, 1999; Belousova et al., 2001; 2002; Chu et al., 2009; Cao et al., 2011; Mazhari and Attar, 2012). The assimilation of reduced sedimentary material in particular has commonly been shown to result in the formation of more reduced and peraluminous silicic granitic magmas (see Takagi, 2004 and references therein). By contrast, apatite in SiO_2-rich metaluminous plutons that attain more silicic compositions by fractional crystallisation alone often show only limited variations in Mn concentration relative to their whole-rocks (see data from Chu et al., 2009, Fig. 6). Redox conditions in these latter plutons are therefore unlikely to have changed significantly during magma evolution. The apparent increase in Mn partitioning in apatite observed under more reducing conditions in a number of plutons therefore appears to be largely independent of the Mn composition of the original melts and may instead depend on other factors such as redox conditions.

Several studies have developed the use of apatite as a provenance indicator based on the different concentrations of Mn and other elements in apatites from different granite sources

(e.g. Sha and Chappell, 1999; Hoskin et al., 2000; Belousova et al., 2001; 2002; Chu et al., 2009). Although links have been drawn between the abundance of Mn in apatites and the redox states of different granitic magmas (e.g. Sha and Chappell, 1999; Belousova et al., 2001; Chu et al., 2009), no attempt has been made to evaluate fO_2 values using apatite Mn concentrations and the extent to which redox proxies in magmatic apatite and zircon are complementary to each other and to other redox proxies.

5.1 Redox and other controls on apatite compositions

Apatite, a common constituent of intermediate to silicic igneous rocks, has the general formula $Ca_{10}(PO_4)_6(OH,F,Cl,Br)_2$ and a crystal structure consisting of rigid PO_4 tetrahedra, a 9-fold Ca1 site and a Ca2 site bonded to six oxygen atoms and one anion (Cl, F, OH). The apatite structure is highly tolerant of structural distortion and chemical substitutions, and can therefore display a wide variety of compositions (Pan and Fleet, 2002), which includes the incorporation of redox-sensitive elements like Mn, Fe and the REEs. The maximum Mn content in natural fluorapatite is 1.37 Mn per formula unit, with Mn^{2+} substituting preferentially onto Ca1 sites (Pan and Fleet, 2002).

In the Criffell pluton the Mn content of apatite increases as ferric iron (Fe^{3+}) decreases in the whole-rock (Fig. 3); the concentration of ferric iron is strongly controlled by the redox state of the magma (Lee et al., 2010 and references therein). More oxidised outer zones (zones 1 and 2) of the pluton formed from magmas with elevated Fe^{3+}/Fe^{2+} (Stephens et al., 1985) which are also likely to have had elevated Mn^{3+}/Mn^{2+}. By contrast, the innermost granites (zones 4 and 5) are characterised by lower whole-rock Fe^{3+} and more reducing conditions. Mn^{2+} exhibits similarities in ionic radius when in 7- (0.9Å) and 9-fold (1.0Å) coordination with Ca^{2+} (1.14Å), with which substitution occurs. By comparison, Mn^{3+} has an ionic radius

of 0.62Å to 0.67Å depending on the degree of distortion, and requires the existence of cation vacancies or the possible substitution of additional charge-balancing ions in the crystal lattice. One possibility may include a coupled substitution such as $Mn^{3+} + Si^{4+} = Ca^{2+} + P^{5+}$ as suggested for the substitution of some REE^{3+} in apatite (Sha and Chappell, 1999) and may in part account for the elevated Si contents of apatites in more oxidised zones (Table 1). To a large extent, the increased compatibility of Mn in apatites from reduced zones of the pluton is likely to result from the increased compatibility of Mn^{2+} relative to Mn^{3+} in these zones. Some spectroscopic data also indicates that Mn^{5+} may substitute for P^{5+}, although the former is likely to represents no more than ~ 5% of total Mn in apatite (Hughes et al., 2004).

5.1.1 Preservation of Mn compositions in apatite

Do variations in Mn in apatite reflect magmatic conditions at the time of crystallisation or later modifications? Assuming an effective diffusion radius of 250µm and temperatures of ~700^{o}C (estimated by Ti-in-zircon thermometry; see Table 2), apatite crystal cores are expected to retain close to initial Mn concentrations on timescales of ~ 10^6 years (Cherniak, 2005). However, silicic plutonic rocks are unlikely to be held at such temperatures for extended periods of time and particularly not when they are assembled incrementally by the emplacement of small melt batches, as is thought to have occurred during development of the Criffell pluton (Miles et al., 2013a). Once cooled to below 600^{o}C, retention times for initial Mn concentration in crystal cores increases to ~10^8 years or more (Cherniak, 2005). Furthermore, a number of the apatite crystals analysed as part of this study have dimensions that are significantly larger than the effective diffusion radius used above. Although some fine-scale intracrystal compositional zoning may be lost, it is reasonable to assume that apatite largely retains Mn concentrations from the time of crystallisation providing subsequent prolonged and extreme thermal events can be ruled out. It is possible that the

absence of significant Mn zoning in apatites from zones 1 and 2 may have resulted from small-scale homogenisation.

5.1.2 Other potential controls on Mn partitioning in apatite

It is also important to explore other potential controls on Mn uptake in apatite that are independent of, or additional to, the effects of redox conditions. Assuming that Mn^{3+} is incompatible in apatite ($D_{Mn3+}^{Ap-melt} = 0$), the observed decrease in $D_{Mn}^{Ap-melt}$ (about 90%) between reduced and oxidised zones may suggest that under the most oxidised conditions, the proportion of Mn that occurs as Mn^{3+} also increases by a similar amount. This seems unlikely based on limited knowledge of redox relations in silicate melts, which suggest that Mn^{3+} represents only a few percent of all Mn (e.g. Schreiber, 1987). Assuming that Mn^{3+} is only moderately incompatible in apatite, but less compatible than Mn^{2+}, may require additional Mn to be present as Mn^{3+}. Thus it is possible that other factors such as temperature, composition and competition with other Mn-bearing minerals may act in addition to redox controls, permitting additional Mn^{3+} to enter the apatite structure at granitic temperatures. Further experimental calibration is needed to fully address these potential issues, but here we examine some of the empirical evidence for other possible controls on the uptake of Mn in apatite.

Temperature controls on Mn partitioning

Published partition coefficient data for Mn in apatite are rare and it remains difficult to fully assess the effects of temperature on Mn partitioning. Apatite is known to crystallise over a range of temperatures in felsic metaluminous magmas because it saturates early relative to other minerals (Piccoli and Candela, 1994; Streck and Dilles, 1998; Miles et al., 2013a). Apatite saturation temperatures (calculated using measured concentrations of SiO_2 and P_2O_5

370 in the whole-rock, Harrison and Watson, 1984; Piccoli and Candela, 1994) vary between
371 912^{o}C and 988^{o}C across all zones of the Criffell pluton, show little variation between zones
372 (Supplementary Material 1) and support the idea of early apatite crystallisation that is
373 consistent with textural evidence showing that most apatite crystals exist as inclusions within
374 other minerals (Miles et al., 2013a). It is suggested that >50% of apatite crystallises within
375 60^{o}C of its liquidus temperature and 90% within 140^{o}C (Piccoli and Candela, 1994; Streck
376 and Dilles, 1998). Individual apatite crystals may therefore represent only part of an extended
377 crystallisation history (Miles et al., 2013a) and further experimental work is required to fully
378 assess the importance of temperature in controlling Mn partitioning in apatite. However, the
379 limited variations in apatite saturation temperatures and textural occurrence of apatites
380 between zones in the Criffell pluton would indicate that other factors, including redox
381 conditions may still exert a strong control on the partitioning of Mn in apatite.
382
383 ***Mineralogical and compositional controls on Mn partitioning in apatite***
384 The presence of other Mn-bearing minerals, such as biotite, amphibole and magnetite, also
385 influence Mn concentrations in apatite insofar as they affect the evolution of melt
386 compositions. It is therefore reasonable to speculate about whether increased concentrations
387 of Mn in apparently more reduced zones reflect the absence of amphibole and the lower
388 abundance of biotite and magnetite in these zones. Published whole-rock data (Stephens et
389 al., 1985) have been used to estimate initial MnO concentrations of 0.06 wt% and 0.05 wt%
390 in oxidised (Zone 1) and reduced (Zone 5) zones respectively. The observed modal
391 proportions (volume proportions) of Mn-bearing minerals (oxidised zones: 1% magnetite,
392 10% biotite, 5% amphibole; reduced zones: 5% biotite) together with published mineral-melt
393 partition coefficients (Latourrette et al., 1991; Ewart and Griffin, 1994; Dawson and Hinton,
394 2003) have been used to calculate the concentrations of Mn available for apatite in the

remaining melt volume after fractional crystallisation of other Mn-bearing minerals that crystallise according to their modal proportions. The maximum 27 fold increase in Mn concentrations observed between apatites in zones 1 and 4 requires >90% crystallisation of both zones prior to the onset of apatite crystallisation (Supplementary Material 4). Late crystallisation of apatite is at odds with textural evidence for the inclusion of apatite in other host minerals and apatite saturation temperatures of >900^{o}C, both of which indicate that apatite crystallised earlier than most other minerals. After more modest levels of fractional crystallisation (~50%), Mn concentrations only increase by a factor of ~ 2 from zones 1 to 4 (Supplementary Material 4). It therefore seems unlikely that the crystallisation of other Mn-bearing minerals will have significantly influenced the uptake of Mn in apatites in the Criffell pluton. A further possibility is that the partitioning of Mn in apatite, or more specifically the activity coefficient of Mn (γMn), is compositionally dependent. Wood and Wade (2013) have recently shown that in silicate melts, the activity coefficient for Fe (γFe) is only very weakly compositionally dependent over a wide range of silicate melt compositions, but further experimental calibration is required to fully examine the influence of melt chemistry and aluminosity on Mn partitioning in apatite.

5.1.3 Other redox proxies in apatite

Fe can constitute up to ~ 1wt % in apatite, and Mössbauer spectroscopy suggests that Fe^{2+} is readily substituted onto both Ca sites (Pan and Fleet, 2002). Despite a lack of published evidence for Fe^{3+} incorporation in apatite, it would appear to be plausible using similar crystal chemistry arguments to those discussed previously for Mn^{3+}. Fe concentrations in apatite are expected to mirror that of Mn, with an increased abundance of Fe in apatite under reduced conditions caused by higher concentrations of more compatible Fe^{2+} in the melt relative to Fe^{3+}. The elevated Fe concentrations measured by electron microprobe in apatites

hosted by Fe-rich minerals is attributed to the effect of secondary fluorescence. Fe analyses of apatites hosted by Fe-poor minerals like quartz and feldspar appear to follow the expected trend, with increased concentrations of Fe in apatites from more reduced zones (Fig. 3b).

Mn/Fe ratios are known not to vary in response to fractional crystallisation in primitive magmas and may thus reveal changes in redox state providing the Mn/Fe ratios of source components are known (Canil et al., 1994; Ruzika et al., 2001). However, in this study and others (Miller and Stoddard, 1981; Cerny et al., 1985; London et al., 2001), granitic suites of rocks show increases in MnO/FeO_{Total} ratios with indices of differentiation like SiO_2. However, this effect is likely to result from the ability of biotite and magnetite to preferentially fractionate Fe ($Kd_{Bt/melt} \approx 25$; $Kd_{Mt/melt} \approx 150$) from Mn ($Kd_{Bt/melt} \approx 5$; $Kd_{Mt/melt} \approx 15$) in silicic magmas. For example, assuming a starting composition similar to that of the most primitive Criffell magma and modal (volume) proportions of magnetite (0.1%) and biotite (10%), Mn/Fe ratios increase by a factor of approximately 10 after 50% fractional crystallisation (Supplementary Material 4). It is therefore difficult to assess the degree to which increases in Mn/Fe seen in apatites from more silicic zones result from redox and/or crystallisation effects.

The ability of Eu to exist in two valency states (Eu^{2+} and Eu^{3+}) may also provide a means of independently estimating the redox state of host magmas. The difference in ionic radius between Eu^{3+} and the Ca^{2+} ions with which it substitutes in apatite is smaller than that between Eu^{2+} and Ca^{2+} in both seven and nine-fold coordination (Cao et al., 2011). Consequently, apatite shows a marked preference for Eu^{3+} relative to Eu^{2+} (e.g. Prowatke and Klemme, 2006). Increasingly negative Eu anomalies in apatites from more silicic zones in the Criffell pluton (Fig. 4) might therefore indicate an increase in Eu^{2+}/Eu^{3+} in those magmas due

446 to more reducing conditions. Additionally, the absence of significant Eu anomalies in whole-
447 rock samples from all zones (Stephens et al., 1985) shows that the observed anomalies in
448 apatite were not inherited from their host magmas, although they could reflect more localised
449 effects during crystallisation, particularly if apatite crystallisation occurred later than most
450 feldspar. The absence of Eu anomalies in whole-rock from granodiorite zones is thought to
451 reflect oxidising conditions, close to the magnetite-hematite buffer (Stephens et al., 1985) or
452 at least more oxidising than NNO+1.5 (Dilles 1987), that did not favour Eu^{2+} partitioning into
453 plagioclase. More reducing redox conditions (close to the NNO buffer) in more silicic zones
454 should have favoured the formation of negative Eu anomalies in the whole-rock due to the
455 uptake of Eu^{2+} by plagioclase (Stephens et al., 1985). Despite this, whole-rock compositions
456 in granitic zones do not exhibit any significant Eu anomalies (Stephenson et al., 1985).
457
458 Whole-rock compositions in the Criffell pluton are thought to have been determined at depth,
459 within a crustal hot zone through fractional crystallisation and assimilation of reduced
460 sedimentary rocks (Miles et al., 2013a; Annen et al., 2006). In this model, low viscosity,
461 H_2O-rich magmas segregate and ascend adiabatically in a super-liquidus state. The absence
462 of Eu anomalies in the granitic zones may therefore reflect resorption of plagioclase during
463 ascent of incremental magma batches prior to final crystallisation at shallower levels (Miles
464 et al., 2013a). Alternatively, redox conditions may only have become significantly more
465 reducing after melt segregation from the crustal hot zone. One possible means of changing
466 oxidation states during differentiation is through the reaction of water with ferrous Fe
467 (Holloway et al., 2004; Lee et al., 2010). This reaction is thought to result in the formation of
468 micro-crystalline magnetite and degassing of H_2, causing possible auto-oxidation. The redox
469 conditions of ascending magmas have also been shown to vary in relation to the amount of

gas in the magma reservoir, with sulphur-rich magmas exhibiting either increases or decreases in redox states that depend on their initial fO_2 (Burgisser and Scaillet, 2007).

Irrespective of why oxidation states vary during differentiation, it is unlikely that feldspar which crystallised at shallow levels either accumulated or was lost from viscous granitic magmas. Despite this, large Eu anomalies may still be induced in coexisting minerals under suitably reducing conditions in the interstitial melt. This effect may explain why co-existing apatite crystals in the most reduced zones (zones 3 and 4) exhibit large negative Eu anomalies (Fig. 4) relative to those in more oxidised zones (zones 1 and 2) of the pluton while whole-rock compositions exhibit little or no negative Eu anomalies. Apatite that crystallises later and at lower temperatures may also exhibit larger negative anomalies due to earlier feldspar crystallisation, though apatite saturation temperatures do not vary appreciably between zones and most apatite in all zones is likely to have crystallised prior to most other minerals.

Unlike zircon, Ce anomalies are not developed in apatites from any zone of the Criffell pluton. This probably reflects the greater compatibility of Ce^{3+} (Ce^{3+} and Ca^{2+} have very similar ionic radii and identical charges) and the extremely low concentration of relatively incompatible Ce^{4+} (Colombini et al., 2011). Unlike zircon, Ce is present almost exclusively as Ce^{3+} in apatite irrespective of redox conditions.

5.2 Redox states determined from Ce/Ce in zircon*

Unlike apatite, the positive Ce anomaly commonly seen in igneous zircon has long been considered to reflect redox conditions in the magma at the time of crystallisation (Hinton and Upton, 1991; Ballard et al., 2002; Trail et al., 2011; 2012; Burnham and Berry, 2012). In a recent experimental study, Trail et al., (2011) calibrated the magnitude of the Ce anomaly

against fO_2 at 900-1300ºC, and applied their method to natural Hadean zircons from Jack Hills (Western Australia) in order to examine the oxidation state of the original host magmas.

The Ce/Ce* values of zircons, and their crystallisation temperatures, from zones 1 to 4 of the Criffell pluton have been used to calculate fO_2 using the experimentally calibrated expression of Trail et al., (2011). The values are reported relative to the fayalite-magnetite-quartz (FMQ) buffer (at standard pressure conditions of 1 bar) for each calculated crystallisation temperature in log units (ΔFMQ) (Fig. 7, Table 2). Each unit represents one log unit deviation in fO_2 from the FMQ buffer, where positive values signify more oxidised conditions and negative values more reduced conditions than those of the buffer. Median ΔFMQ values decrease steadily from +2.5 to +2 to -0.8 to -2 log unit deviations from the FMQ buffer in zones 1 to 4 respectively (Fig. 7). However, there is also significant intra-sample scatter, with interquartile ranges up to ~ 10 log units in Zone 4, similar to those reported by Trail et al., (2011) for the Bishop Tuff.

It is questionable whether large variations in Ce/Ce* (and therefore fO_2) calculated for natural samples in both studies reflect real variations in redox conditions. Variations in Ce/Ce* may result either from changes in the partitioning of Ce into zircon, that in turn reflect redox conditions, or from changes in the relative concentrations of La and Pr. The latter effect is particularly problematic in zircon due to the naturally low concentrations of La and Pr, making LREE analyses especially susceptible to beam overlap with small LREE-rich inclusions (Nagasawa, 1970; Colombini et al., 2011; Trail et al., 2012). One way of testing these interpretations is to use independent proxies for both effects. Sm in zircon is insensitive to redox effects and is found at sufficiently high concentrations in zircon that inclusions of LREE-rich minerals would have only a negligible effect. In an attempt to avoid the effects of

LRRE-rich inclusions in zircon, Ballard et al. (2002) suggest that La and Pr concentrations in apatite may be estimated by extrapolation of zircon HREE chondrite-normalised patterns. However, some suggest that the partitioning of LREE into zircon may be limited by different factors to those that control the partitioning of HREE (Finch et al., 2001; Hanchar et al., 2001). There is no suggestion that the partitioning of Sm into zircon is limited by different factors to those that control the partitioning of LREE. La/Sm ratios in zircon therefore provide a proxy for the presence of LREE-rich inclusions like allanite and monazite, while Ce/Sm ratios reflect changes in the partitioning of Ce into zircon caused by redox changes; the use of ratios in both cases negates the effects of varying magma compositions. For natural samples from this study and the Bishop Tuff (Reid et al., 2011), there is a clear tendency for Ce/Ce* to reflect variations in the concentrations of LREE other than Ce (Fig. 8). By contrast, there is no such tendency for Ce/Ce* to correlate with La and Pr in synthetic zircons used by Trail et al., (2011) to experimentally calibrate their oxybarometer, which instead reflects real variations in the partitioning of Ce into zircon under different redox conditions.

Measured concentrations of LREE in natural zircons vary significantly (Hanchar and van Westrenen, 2007), and it is estimated that inclusion concentrations as low as 0.01 to 0.001 volume % may have a significant effect on the measured LREE content of zircon (Jain et al., 2001). Small amounts of allanite and/or monazite found in heavy mineral separates prepared from samples from all zones of the Criffell pluton support the possibility that small inclusions may be present in zircons, and may in part account for the larger scatter in fO_2 values calculated from Ce/Ce*. In addition, ion microprobe analyses of LREE concentrations in zircons are close to background levels (see Methods) and may result in further errors when calculating Ce/Ce* values. Although the experimental calibration of Trail et al., (2011) provides an important new approach to oxybarometry, conventional methods of calculating

Ce/Ce* in natural zircons remain subject to large uncertainties such as those evident in Figure 7. The method adopted in Figure 8 may provide a general approach to assessing and interpreting REE analyses of natural zircons by micro-analytical techniques and recognising the possible impact of small mineral inclusions on analyses.

5.3 Preliminary calibration of an apatite Mn oxybarometer

To investigate the potential of using Mn concentrations in apatites as a magma oxybarometer and redox proxy, we have used a range of examples where apatite compositions are available together with independent estimates of redox conditions. The average concentration of Mn in apatites from eight intermediate and silicic volcanic eruptions are summarised by Peng et al. (1997) whilst Scaillet et al., (1998) documented redox conditions for a number of these eruptions. For the Criffell pluton, Fe^{3+}/Fe^{2+} in biotites from granodiorite and granite samples indicate fO_2 values that are close to the magnetite-hematite and NNO buffers respectively (Stephens et al., 1985). Apatite Mn concentrations in all samples fall along a consistent trend, where Mn concentrations show a strong negative linear correlation with log fO_2 (R^2 = 0.9, Fig. 9) according to the following relationship:

$$\log fO_2 = -0.0022(\pm 0.0003)\ \text{Mn (ppm)} - 9.75(\pm 0.46)$$

This preliminary empirical calibration is likely to apply to systems that lie within the range of eruption temperatures (660 - 920^{o}C, Supplementary Material 5) and compositions (andesite to rhyolite) shown by these data. Direct experimental calibration of this oxybarometer is now required in order to provide a more robust proxy than zircon for determining redox conditions in intermediate and silicic magmas and to properly examine the controls on Mn partitioning in apatite. Despite the remaining uncertainties in understanding the relative importance of

redox and other potential controls on Mn partitioning in apatite, empirical evidence from natural samples indicate that it is a useful proxy for assessing the degree of oxidation across a wide range of intermediate to silicic magmas.

6. Wider applications of an apatite oxybarometer

Apatite may be of particular value in reconstructing the redox conditions of intermediate and silicic eruptions where redox conditions are known to strongly influence emissions of climatically important elements such as sulphur (Scaillet et al., 1998; Robock, 2000). In the presence of only 1-5 wt % fluid, there is a marked preference for sulphur to partition into the fluid rather than the melt under oxidising conditions (fO_2 >NNO+1, Scaillet et al., 1998). Excess sulphur generated in this way may account for the discrepancy between the amount of sulphur actually measured in emissions and the amount of sulphur in emissions that is expected from melt degassing calculations, and may also ensure that oxidised, explosive silicic eruptions like Fish Canyon (21.8 Ma, fO_2 ~ NNO + 2, Johnson and Rutherford, 1989) are of significant climatic importance. Many eruptions where calculated fO_2 values suggest oxidising conditions, such as the 1991 Pinatubo eruption, also contain apatites that are only marginally more enriched in Mn than their host magmas (Peng et al., 1997; Van Hoose et al., 2013) and provide further credence that Mn in apatite may be a reliable proxy for redox conditions. By contrast, similarly voluminous but more reduced eruptions such as at Toba (74,000 yrs, fO_2 < NNO + 1, Chesner, 1998; Scaillet et al., 1998) are thought to have had a more limited climatic impact because sulphur was largely fixed in sulphur-bearing pyrrhotite. Other explosive eruptions of large magnitude, such as that which produced the Bishop Tuff, also involved reduced, cool silicic magmas and may also have had negligible long-term (years to centuries) atmospheric effects (Scaillet et al., 1998). This conclusion is supported by evidence that apatites in these magmas are up to seven times richer in Mn than the host

whole-rock (data from Peng et al., 1997 and Hildreth et al., 1979). Assessing the effects that different eruptions have had on Earth's atmosphere therefore depend on understanding how the redox state of magmas has varied through geological history. Apatite provides a potentially valuable way of assessing this in a range of intermediate to silicic magmas.

The isotopic record of terrestrial detrital accessory minerals has proved central to many studies of the early evolution of the continental crust (e.g. Eiler, 2007; Kemp et al., 2006, 2007; Hawkesworth et al., 2010; Wilde et al., 2001). Detrital accessory minerals may also offer insights into the redox states of magmas lost from the geological record, such as those of the Archean and Hadean eons (Lee et al., 2010; Trail et al., 2011). Like zircon, apatite is a prevalent and robust accessory phase in the detrital record (Morton and Yaxley, 2007; Corfu and Easton, 2001; Chamberlain and Browning, 2001), and is commonly preserved as an inclusion phase in a range of host minerals in even the most re-worked sediments. Although the context of the original host rocks is now lost, the observed magnitude of variation in Mn concentrations in apatites from oxidised and reduced magmas means it should be possible to constrain the redox condition of host magmas from detrital grains alone.

Acknowledgements

AM is grateful to NERC for a CASE studentship and acknowledges the support of the British Geological Survey for a BUFI grant to meet the costs of analytical work. NERC is also thanked for use of the Edinburgh Ion Microprobe Facility. John Craven has provided valuable assistance during ion probe analyses. Chris Hayward is thanked for his assistance with electron probe analyses of apatite and Mike Hall for support with zircon mounts and thin section preparation. Ian Butler provided valuable assistance with reflected light microscopy. We thank Godfrey Fitton and Nigel Harris for helpful comments on early drafts of the

manuscript. Calvin Miller, Antony Burham and John Dilles have provided helpful reviews that have greatly improved the manuscript. We also thank Ed Ripley for his editorial handling.

Figures

Fig. 1 a) Regional distribution of major Scottish plutons. Abbreviations: HBF – Highland Boundary Fault, IS – Iapetus Suture. b) Map of the Criffell pluton. Paler shading reflects increasing whole-rock SiO_2. Compositional contours are from Stephens and Halliday (1980). Zone lithologies as follows (minerals listed in order of increasing modal abundance): 1) clinopyroxene-biotite-hornblende granodiorite; 2) biotite-hornblende granodiorite; 3) biotite granite; 4) biotite-muscovite granite 5) muscovite-biotite granite (Stephens et al., 1985). Black points denote sample sites with the following sample numbers: Zone 1 – AM0917, Zone 2 – AM0918, Zone 3 – AM0921, Zone 4 – AM0922.

Fig. 2 Back-scatter Scanning Electron Microscope (SEM) image of magnetite with trellis-like oxidation-exsolution lamellae from Zone 3 of the Criffell pluton. This is likely to reflect exsolution of magnetite and ulvospinel, with subsequent oxidation of ulvospinel to ilmenite (Haggerty, 1991). Exsolution lamellae are not seen in magnetite from other, less silicic zones.

Fig. 3 a) Mn concentrations (re-calculated as ppm) in zones 1 to 4 of the Criffell pluton. Whole-rock Mn concentrations decrease from outer (Zone 1) to inner (Zone 4) zones while apatite Mn concentrations increase, reflecting increasingly compatible substitution of Mn into apatite. b) Fe_2O_3 concentrations in zones 1 to 4 of the Criffell pluton. Fe-poor host minerals are zircon, feldspar and quartz, Fe-rich minerals are biotite and hornblende. The general

decrease in whole-rock Fe^{3+} towards more silicic zones is evident along with a general increase in apatites hosted by Fe-poor minerals. Apatites hosted by Fe-rich minerals have higher Fe concentrations due to secondary fluorescence during EPMA analysis. The data for apatites hosted by Fe-poor minerals exclude four anomalously high values. c) MnO/FeO_{Total} in zones 1 to 4 of the Criffell pluton. Apatite values are for those hosted in Fe-poor minerals only, and exclude the same anomalous values as in (b). EPMA 2σ analytical error on Mn concentrations in apatite is ~ ±150 ppm.

Fig.4 Calculated Eu anomalies ($Eu/Eu^* = Eu_N/(Sm_N \times Gd_N)^{1/2}$) for apatites from zones 1 to 4 of the Criffell pluton.

Fig. 5 a) Average chondrite-normalised zircon REE profiles for zones 1 to 4 of the Criffell pluton. b) Zircon Ce anomalies $Ce/Ce^* = Ce/(La_N \times Pr_N)^{1/2}$ for individual zircon crystals from zones 1 to 4 of the Criffell pluton. Median values for each zone are represented by star symbols and error bars represent interquartile ranges. Compositions determined using a Cameca 4f ion microprobe at the University of Edinburgh.

Fig. 6 Apatite MnO/whole-rock MnO vs. Whole-rock SiO_2 for different suites of granitic (SiO_2 > 63wt %) rocks. Increasing apatite/ whole-rock Mn ratios in more silicic samples are evident. Samples that have ratios < 5 when whole-rock SiO_2 > 70% (e.g. samples from Belousova et al., 2001; Chu et al., 2009) are typically from fractionated I-type granites with only minor volumes of assimilated reduced sedimentary rocks. The redox state of these magmas is likely to have remained more oxidising than in S-type magmas.

Fig. 7 Oxygen fugacity values calculated using the expression of Trail et al., (2011) plotted as log unit deviations from the fayalite-magnetite-quartz (FMQ) buffer (Frost, 1991) (ΔFMQ). Horizontal lines represent median values and the upper and lower box boundaries represent interquartile ranges. Error bars represent 1.5 times the interquartile range and data points outside of these regions are considered outliers. Upper mantle oxygen fugacities are from Delano, 2001; Mallmann and O'Neill, 2009 and Frost and McCammon, 2008.

Fig. 8 La/Sm and Ce/Sm plotted against Ce/Ce* for zircons from the Criffell pluton (this study) and Bishop Tuff (Reid et al., 2011). A clear power law relationship is evident between Ce/Ce* and La/Sm, suggesting that variations in Ce/Ce* and calculated fO_2 are more strongly dependent on relative changes in the concentrations of La and Pr rather than Ce.

Fig. 9 Average apatite Mn concentrations for different volcanic eruptions (black symbols) against independent estimates of oxygen fugacity (fO_2). Oxygen fugacities have been calculated using the NNO buffer equation of Eugster and Wones (1962) at the eruption temperatures listed by Scaillet et al., (1998) for each volcano. For the Criffell samples (grey symbols), redox estimates are from Stephens et al., (1985) and converted to fO_2 using temperature estimates obtained from Ti-in-zircon thermometry (Table 2). Horizontal error bars represent 1 standard deviation in average apatite Mn concentrations. Apatite data together with sample details can be found in Peng et al. (1997) and references therein, redox data are from Scaillet et al., (1998) and references therein. Numbers adjacent to data points denote the following intrusions and volcanoes: 1 – Criffell granodiorite (Zone 1), 2 – Mount St Helens (May 18, 1980 eruption), 3 – Láscar, 4 – Tambora, 5 – Krakatau, 6 – El Chichón, 7 – Pinatubo, 8 – Bishop Tuff, 9 – Santa Maria, 10 – Criffell granite (Zone 4). See Appendix 1

694 in Peng et al., (1997) for sample details. Eruption temperatures reported in Supplementary
695 Material 5.
696
697 Supplementary Material 1: Whole-rock compositions from Stephens and Halliday (1980) and
698 apatite saturation temperatures
699 Supplementary Material 2: Compositional traverses of apatite crystals in Zones 1 and 2
700 Supplementary Material 3: Ims-4f SIMS apatite analyses reported in ppm
701 Supplementary Material 4: Fractional crystallisation models
702 Supplementary Material 5: Temperature, SiO_2 and redox conditions for volcanic samples
703
704
705 **REFERENCES CITED**
706
707 Annen, C., Blundy., J. and Sparkes, S.J. (2006) The genesis of intermediate and silicic
708 magmas in deep crustal hot zones. J. Petrol **47**, 505-539.
709
710 Arculus, J.R. (2003) Use and abuse of the terms calcalkaline and calcalkalic. J.Pet. **44**, 929-
711 935.
712
713 Ballard J.R., Palin, J.M. and Campbell, I.H. (2002) Relative oxidation states of magmas
714 inferred from Ce(IV)/Ce(III) in zircon: application to porphyry copper deposits of northern
715 Chile. Contrib. Min. and Pet. **144**, 347-364.
716

717 Belousova, E.A., Walters, S., Griffin, W.L. and O'Reilly, S.Y. (2001) Trace-element
718 signatures of apatites in granitoids from the Mt Isa Inlier, northwestern Queensland. Aust. J.
719 Earth. Sci. **48**, 603-619.
720
721 Belousova, E.A., Griffin, W.L., O'Reilly, S.Y., and Fisher, N.I. (2002) Apatite as an indicator
722 mineral for mineral exploration: trace-element compositions and their relationship to host
723 rock type. J. Geochem. Explo. **76**, 45-6.
724
725 Belvin, P.L. (2004) Redox and compositional parameters for interpreting the granitoid
726 metallogeny of Eastern Australia: Implications for gold-rich ore systems. Resour. Geol. **54**,
727 241-252.
728
729 Binder, B and Keppler, H. (2011) The oxidation state of sulphur in magmatic fluids. Earth
730 Planet Sci. Lett. **301**, 190-198.
731
732 Burgisser, A and Scaillet, B. (2007) Redox evolution of a degassing magma rising to the
733 surface. Nature **445**, 194-197.
734
735 Burnham, A.D. and Berry, A.J. (2012) An experimental study of trace element partitioning
736 between zircon and melt as a function of oxygen fugacity. Geochim. Cosmochim. Acta **95**,
737 196-212.
738
739 Canil, D., O'Neill, H. St.C., Pearson, D.G., Rudnick, R.L., McDonough, W.F., Carswell,
740 D.A. (1994) Ferric iron in peridotites and mantle oxidation states. Earth Planet Sci. Lett. **123**,
741 205-220.

Canil, D. (1997) Vanadium partitioning and the oxidation state of Archean komatiite magmas. Nature **389**, 842-845.

Carmichael, I.S.E. (1991) The redox state of basic and silicic magmas: a reflection of their source regions? Contrib. Mineral. Petrol. **106**, 129-141.

Carmichael, I.S.E., and Ghiorso, M.S. (1990) The effect of oxygen fugacity on the redox state of natural liquids and their crystallising phases. Rev. Mineral. **24**, 191-2012.

Cao, M., Li, G., Qin, K., Seitmuratova, E.Y. and Liu, Y. (2011) Major and trace element characteristics of apatites in granitoids from Central Kazakhstan: Implications for petrogensis and mineralization. Resour. Geol. **62**, 63-83.

Cerny, P., Meintzer, R.E., Anderson, A.J. (1985) Extreme fractionation in rare-element granitic pegmatites: selected examples of data and mechanisms. Can. Mineralo. **23**, 381-421.

Chamberlain, K.R. and Browning, S.A. (2000) Apatite-feldspar U-Pb thermochronometer: a reliable mid-range (~450^{o}C), diffusion controlled system. Chem. Geol. **172**, 173-200.

Cherniak, D.J. and Watson, B.W. (2003) Diffusion in zircon. In Zircon (eds. Hanchar, J.M., and Hoskin, P.W.O) Mineral. Soc. Am, p. 113-139.

Cherniak, D.J. (2005) Uranium and manganese diffusion in apatite. Chem. Geol. **219**, 297-308.

Chesner, C.A. (1998) Petrogenesis of the Toba tuffs, Sumatra, Indonesia. J. Petrol. **39**, 397-438.

Chu, M.F., Wang K.L., Griffin, W.L., Chung, S.L., O'Reilly, S.Y., Pearson, N.J., Lizuka, Y, (2009) Apatite composition: Tracing petrogenetic processes in Transhimalayan granitoids. J. Petrol. **50**, 1829-1855.

Claiborne, L.L., Miller, C.F., Wooden, J.L. (2010) Trace element composition of igneous zircon: a thermal and compositional record of the accumulation and evolution of a large silicic batholith, Spirit Mountain, Nevada. Contrib. Mineral. Petrol. **160**, 511-531.

Colombini, L.L., Miller, C.F., Gualda, G.A.R, Wooden, J.L., Miller, J.S. (2011) Sphene and zircon in the Highland Range volcanic sequence (Miocene, southern Nevada, USA): elemental partitioning, phase relations, and influence on evolution of silicic magma. Contrib. Mineral. Petrol. **102**, 29-50.

Corfu, F. and Easton, R.M. (2001) U-Pb evidence for polymetamorphic history of Huronian rocks within the Grenville front tectonic zone east of Sudbury, Ontario, Canada: Chem. Geol. **172**, 2979-2995.

Dawson, J. and Hinton, R. (2003) Trace-element content and partitioning in calcite, dolomite, and apatite in carbonate, Phalaborwa, South Africa. Min. Mag. **67**, 921-930.

791 Delano, J.W. (2001) Redox history of the Earth's interior since ~3900 Ma: implications for
792 prebiotic molecules. Origins of Life and Evolution of Biospheres **31**, 311-341.
793
794 Dilles, J.H. (1987) Petrology of the Yerington batholith, Nevada: Evidence for evolution of
795 porphyry copper ore fluids. Econ Geol 82, 1750-1789.
796
797 Eiler, J. M. (2007) On the origins of granites. Science **315**, 951-952.
798
799 Eugster, H. P. and Wones, D. R. (1962) Stability relations of the ferruginous biotite, annite. J.
800 Petrol. **3**, 82-125.
801
802 Ewart, A. and Griffin, W.L. (1994) Application of Proton-Microprobe Data to Trace-Element
803 Partitioning in Volcanic-Rocks. Chem. Geol. **117**, 251-284.
804
805 Ferry, J.M., and Watson, E.B. (2007) New thermodynamic models and revised calibrations
806 for the Ti-in-zircon and Zr-in-rutile thermometers. Contrib. Mineral. Petrol. **154**, 429-437.
807
808 Finch, R.J., Hanchar., J.M., Hoskin, P.O. and Burns, P.C. (2001) Rare-earth elements in
809 synthetic zircon: Part 2. A single-crystal X-ray study of xenotime substitution. Am Mineral.
810 **86**, 681-689.
811
812 Frost, D.J. and McCammon, C.A. (2008) The redox state of Earth's mantle. Ann. Rev. Earth
813 Planet. Sci. **36**, 289-420.
814

Frost, R.B. (1991) Introduction to oxygen fugacity and its petrological importance. In: Lindsley, D.H. (ed): Oxide minerals: petrologic and magnetic significance. Rev. Mineral **25**, 1-8.

Ghiorso, M.S. and Gualda, G.A.R. (2013) A method for estimating the activity of titania in magmatic liquids from the compositions of existing rhombohedral and cubic iron-titanium oxides. Contrib Mineral Petrol **165**, 73-81.

Gill, J.B. (1981) Orogenic Andesites and Plate Tectonics. Springer.

Gonnerman, H.M. and Manga, M. (2003) Explosive volcanism may not be an inevitable consequence of magma fragmentation. Nature **426**, 423-435.

Haggerty, S. (1991) Oxide textures. A mini atlas. In: Lindsley, D.H. (eds) Oxide minerals: petrologic and magnetic significance. Min Soc Am, Rev Mineral 25, Chapter 5: 129-219

Hanchar, J.M., Finch, R.J., Hoskin, P.O., Watson, E.B., Cherniak, D.J. and Mariano, A.N. (2001) Rare earth elements in synthetic zircon: Part 1. Synthesis, and rare-earth element and phosphorus doping of zircon. Am. Mineral. **86**, 667-680.

Hanchar, J.M and van Westrenen, W. (2007) Rare earth element behaviour in zircon-melt systems. Elements **3**, 37-42.

Harrison, T.M. and Watson, E.B. (1984) The behaviour of apatite during crustal anatexsis: equilibrium and kinetic considerations. Geochim. Cosmochim. Acta **48**, 1467-1477.

Hawkesworth, C. J., Dhuime, B., Pietranik, A.B., Cawood, P.A., Kemp, A.I.S., and Storey, C.D. (2010) The generation and evolution of the continental crust: Journal of the Geological Society **167**, p. 229-248.

Hayden L.A., and Watson, E.B. (2007) Rutile saturation in hydrous silicate melts and its bearing on Ti-thermometry of quartz and zircon. Earth Planet. Sci. Lett. **258**, 561-568.

Hayden, LA., Watson, E.B., Wark, D.A. (2008) A thermobarometer for sphene (titanite). Contrib Mineral Petrol **155**, 529-540.

Hildreth, W. (1979) The Bishop Tuff: Evidence for the origin of compositional zonation in silicic magma chambers. Geol. Soc. Am. Special Papers **180**, 43-76.

Hinton, R.W. and Upton, B.G. (1991) The chemistry of zircon: Variations within and between large crystals from syenite and alkali basalt xenoliths. Geochim. Cosmochim Acta **55**, 3287-3302.

Holloway, J.R. (2004) Redox in seafloor basalts: possible insights into silicic hydrothermal systems. Chem Geol 210 p. 225-230.

Hoskin, P.W., Kinny, P.D., Wyborn, D., et al., (2000) Identifying accessory mineral saturation during differentiation in granitoid magmas: an integrated approach. J. Petrol.**41**,1365-1396.

865 Hoskin, P.W. and Schalegger, U. (2003) The composition of zircon and igneous and
866 metamorphic petrogensis. In, Hanchar, J.M. and Hoskin, P.W.O. (eds) Zircon. Rev. Mineral.
867 Geochem. **53**, 27-62.
868
869 Hughes, J.M., Ertle, A., Bernhardt, H.J., Rossman, R.J. (2004) Mn-rich fluorapatite from
870 Ausria: Crystal structure, chemical analysis, and spectroscopic investigations. Am. Mineral.
871 **89**, 629-632.
872
873 Huppert, H.E. and Woods, A.W. (2002) The role of volatiles in magma chamber dynamics.
874 Nature **420**, 493-495.
875
876 Ishihara, S. (1977) The magnetite-series and ilmenite-series granitic rocks. Mining Geology,
877 **27**, p. 293-305.
878
879 Ishihara, S. (1981) The granitoid series and mineralization. Econ. Geol. 75th Anniversary
880 Volume, p. 458-484.
881
882 Ishihara, S. (2004) The redox state of granitoids relative to tectonic setting and earth history:
883 The magnetite-ilmenite series 30 years later. Trans.R Soc. Edin. Earth Sci, **95**, 23-33.
884
885 Jain, J.C., Neal, C.R., Hanchar, J.M. (2001) Problems associated with the determination of
886 rare earth elements of a “gem” quality in zircon by inductively coupled mass-spectrometry.
887 Geostandards Newsletter **25**, 229-237.
888

889 Johnson, M.C. and Rutherford, M.J. (1989) Experimentally determined conditions in the Fish
890 Canyon tuff, Colorado, magma chamber. J.Petrol **3**, 711-737.
891
892 Kasting, J.F., Eggler, D.H. and Raeburn, S.P. (1993) Mantle redox evolution and the
893 oxidation state of the atmosphere. J. Geol. **101**, 245-257.
894
895 Kelly, K.A., and Cottrell, E. (2009) Water and the oxidation state of subduction zone
896 magmas. Science **325**, 605-607.
897
898 Kemp, A.I.S., Hawkesworth, C.J., Paterson, B.A., Kinny, P.D. (2006) Episodic growth of the
899 Gondwana supercontinent from hafnium and oxygen isotopes in zircon. Nature **439**, 580-583.
900
901 Kemp, A. I. S., Hawkesworth, C.J., Foster, G.L., Paterson, B.A., Woodhead, J.D., Hergt,
902 J.M., Gray, C.M., and Whitehouse M.J. (2007) Magmatic and crustal differentiation history
903 of granitic rocks from Hf-O isotopes in zircon. Science **315**, 980-983.
904
905 Latourrette, T.Z., Burnett, D.S. and Bacon, C.R. (1991) Uranium and minor-element
906 partitioning in Fe-Ti oxides and zircon from partially melted granodiorite, Crater Lake,
907 Oregon. Geochim Cosmochim Acta **55**, 457-469.
908
909 Lee, C.A., Luffi, P., Le Roux, V., Dasgupta, R., Albaréde, F. and Leeman, W.P. (2010) The
910 redox state of arc magmas using Zn/Fe systematics. Nature **468**, 681-685.
911

912 Llovet, X. and Galan, G. (2003) Correction of secondary X-ay fluorescence near grain
913 boundaries in electron microprobe analysis: Application to thermombarometry of spinel
914 lherzolites. Am Mineral **88**, 121-130.
915
916 London, D., Evensen, J.M, Fritz, E., Icehower, J.P., Morgan, G.B. VI., Wolf, M.B. (2001)
917 Enrichment and accommodation of manganese in granite-pegmatite systems. 11th Annual
918 Goldschmidt Conference Abstract 3369.
919
920 Mallmann, G. and O'Neill, H.S.C. (2009) The crystal/melt partitioning of V during mantle
921 melting as a function of oxygen fugacity compared with some other elements (Al, P, Ca, Sc,
922 Ti, Cr, Fe, Ga, Y, Zr and Nb). J.Petrol. **50**, 1765-1794.
923
924 Mazhari, S.A. and Attar, R.S. (2012) Apatite application to investigate magmatic evolution of
925 Zouzan granites, NE Lut Block. Iranian J. Earth Sci. **4**, 61-72.
926
927 Miles, A.J., Graham, C.M., Hawkesworth, C.J., Gillespie, M.R., Hinton, R.W. and EIMF
928 (2013a) Evidence for distinct stages of magma history recorded by the compositions of
929 accessory apatite and zircon. Contrib. Mineral Petrol **166**, 1-19.
930
931 Miles, A.J., Graham, C.M., Hawkesworth, C.J., Gillespie, M.R., Dhuime, B. and Hinton,
932 R.W. (2013b) Using zircon isotope compositions to constrain crustal structure and pluton
933 evolution: the Iapetus suture zone granites in Northern Britain. J. Petrol, doi:
934 10.1093/petrology/egt065.
935

936 Miller, C.F. and Stoddard, E.F. (1981) The role of manganese in the paragenesis of magmatic
937 garnet: An example from the Old Woman-Piute Range, California. J. Geol **89**, 233-246.
938
939 Morton, A. and Yaxley, G. (2007) Detrital apatite geochemistry and its application in
940 provenance studies. GSA Special Paper **420**, 319-344.
941
942 Nagasawa, H. (1970) Rare earth concentrations in zircons and apatites and their host dacites
943 and granites. Earth Planet. Sci. Lett. **9**, 359-364.
944
945 Pan, Y.M and Fleet, M.E. (2002) Compositions of the apatite-group minerals: Substitution
946 mechanisms and controlling factors. In Phosphates: Geochemical, Geobiological, and
947 Materials Importance (eds. Kohn, M.J., Rakovan, J, and Hughes, J.M.) Mineral. Soc. Am. p.
948 13-49.
949
950 Pearce N.J.G., Perkins W.T., Westgate J.A., Gorton M.P., Jackson S.E., Neal C.R. and
951 Chenery S.P. (1997) A compilation of new and published major and trace element data for
952 NIS T SRM 6 10 and NIST SRM 6 12 glass reference material Geostandards Newsletter. The
953 Journal of Geostandards and Geoanalysis, **21**, 115-144.
954
955 Peng, G. Luhr, J.F. and McGee, J.J. (1997) Factors controlling sulphur concentrations in
956 volcanic apatite. Am. Mineral. **82**, 1210-1224.
957
958 Piccoli, P.M. and Candela, P.A. (1994) Apatite in felsic rocks: a model for the estimation of
959 initial halogen contents in the Bishop Tuff (Long Valley) and Tuolumne Intrusive Suite
960 (Sierra Nevada Batholith) Magmas. Am J of Sci, **294**, 92- 135.

961

962 Pidgeon, R.T. and Aftalion, M. (1978) Cogenetic and inherited zircon U-Pb systems in
963 granites: Palaeozoic granites of Scotland and England, in Bowes, D.R., Leake, B.E., Crustal
964 evolution in northwestern Britain and adjacent regions. Geological Journal Special Issues, p.
965 183-220.

966

967 Prowatke, S. and Klemme, S. (2006) Trace element partitioning between apatite and silicate
968 melts. Geochim Cosmochim Acta **70**, 4,513-4,527.

969

970 Reid, M.R., Vazquez, J.A. and Schmitt, A.K (2011) Zircon-scale insights into the history of a
971 Supervolcano, Bishop Tuff, Long Valley, California, with implications for the Ti-in-zircon
972 geothermometer. Contrib. Mineral Petrol **161**, 293-311.

973

974 Riley, J.P. (1958) Rapid analysis of silicate rocks and minerals. Anlaytica Chimica Acta **19**,
975 413-428.

976

977 Robock, A. (2000) Volcanic eruptions and climate. Rev Geophys. **38**, 191-219.

978

979 Ruzika, A., Snyder, G.A., Taylor, L.A. (2001) Comparative geochemistry of basalts from the
980 Moon, Earth, HED asteroid, and Mars: implications for the origin of the Moon. Geochim.
981 Cosmochim Acta **65**, 979-997.

982

983 Scaillet, B. and Gaillard, F. (2011) Redox state of early magmas. Nature **480**, 48-49.

984

985 Scaillet, B., Clemente, B., Evans, B.W., Pichavant, M. (1998) Redox control of sulphur
986 degassing in silicic magmas. J. Geophys. Res. **103**, 23,937-23,949.
987
988 Sha, L. K. and Chappell, B.W. (1999) Apatite chemical composition, determined by electron
989 microprobe and laser-ablation inductively coupled plasma mass spectrometry, as a probe into
990 granite petrogenesis. Geochim Cosmochim Acta **63**, 3861-3881.
991
992 Schreiber, H.D., Merkel, R.C., Schreiber, V.L. and Balazs, G.B. (1987) Mutual interactions
993 of redox couples via electron exchange in silicate melts: Models for geochemical melt
994 systems. J. Geophys. Res. **92**, 9233-9245.
995
996 Stephens, W.E. and Halliday., A.N. (1980) Discontinuities in the composition surface of a
997 zoned pluton, Criffell, Scotland. Geol. Soc.Am. Bull. **91**, 165-170.
998
999 Stephens, W. E., Whitley, J. E., Thirlwall, M.F. and Halliday, A. N. (1985) The Criffell
1000 zoned pluton: correlated behaviour of rare earth element abundances with isotopic systems.
1001 Contrib. Mineral. Petrol. **89**, 226-238.
1002
1003 Streck, M.J. and Dilles, J.H. (1998) Sulfur evolution of oxidised arc magmas as recorded in
1004 apatite from a porphyry copper batholith. Geology **26**, 523-526.
1005
1006 Takagi, T. (2004) Origin of magnetite- and ilmenite-series granitic rocks in the Japan Arc.
1007 Am J Sci **304**, 169-202.
1008

1009 Thomas, J.B., Watson, E.B., Spear, F.S., Shemella, P.T., Nayak, S.K., Lanzirotti, A. (2010)
1010 TitaniQ under pressure: the effect of pressure and temperature on the solubility of Ti in
1011 quartz. Contrib Mineral Petrol **160**, 743-759.
1012
1013 Trail, D., Watson, B.E. and Tailby, N.D. (2011) The oxidation state of Hadean magmas and
1014 implications for early Earth's atmosphere. Nature **480**, 79-81.
1015
1016 Trail, D., Watson, B.E. and Tailby, N.D. (2012) Ce and Eu anomalies in zircon as proxies for
1017 the oxidation state of magmas. Geochim. Cosmochim. Acta **97**, 70-87.
1018
1019 Van Hoose, A.E., Streck, M.J., Pallister, J.S. and Wälle, M. (2013) Sulfur evolution of the
1020 1991 Pinatubo magmas based on apatite. J.Volcan. Geotherm. Res. **257**, 72-89.
1021
1022 Wark, D.A. and Watson, E.B. (2006) TitaniQ: a titanium-in-quartz geothermometer. Contrib
1023 Mineral Petrol **152**:743-754.
1024
1025 Weill, D.F. and Drake, M.J. (1973) Europium anomaly in plagioclase feldspar: Experimental
1026 results and semi-quantitative model. Science **180**, 1059–1060.
1027
1028 Wiedenbeck, M., Hanchar, J.M., Peck, W.H., Sylvester, P., Valley, J., Whitehouse, M.,
1029 Kronz, A., Morishita, Y., Nasdala, L. et al., (2004) Further characterization of the 91500
1030 zircon crystal. Geostandards and Geoanalysis **28**, 9-39.
1031

Wilde, S.A., Valley, J.W., Peck, W.H and Graham, C.M. (2001) Evidence from detrital zircon for the existence of continental crust and oceans on Earth 4.4 Gyr Ago. Nature **409**, 175-178.

Wones, D.R. (1989) Significance of the assemblage titanite + magnetite + quartz in granitic rocks. Am Mineral **74**, 744-749.

Wood, B.J. and Wade, J. (2013) Activities and volatiles of trace components in silicate melts: a novel use of metal-silicate partitioning data. Contrib. Mineral. Petrol. **166**, 911-921.

Xirouchakis, D., Lindsey, D.H. and Andersen, D.J. (2001) Assemblages with titanite ($CaTiOSiO_4$), Ca-Mg-Fe olivine and pyroxenes, Fe-Mg-Ti oxides, and quartz: Part I. Theory. Am Mineral **86**, 747-753.

Table 1

Table 1 -Element concentrations in apatite. Electron probe (Cameca SX-100) analyses (black) reported as ppm and calculated from

Zone	Sample	Host	F	Na	Ca	P	Si	Mg	Cl	Mn	Fe	Sr	Y	La	Ce
1	17A_2	Zrc	25872		379757	173257	5804	39	391	246		737	330	492	1423
	17A_25	Zrc	28957		386385	181404	1716	21		281	148	711	269	1855	3352
	17A_43	Zrc	23658	554	390118	176133	1786	47	337	323	245	462	155	1109	2150
	17A_43_2	Zrc	25805		390415	177065	1592	43	147	433	158	459	367	1444	2916
	17A_60	Zrc	29115		386571	176680	3252	52	306	426		503	358	970	2228
	17A_93	Zrc	*26900*	*521*	*400220*	*195500*	*3951*		*954*			*536*	*388*	*1353*	*3012*
	17A_93	Zrc	*29838*	*502*	*400220*	*213520*	*2781*		*903*			*501*	*385*	*1310*	*2965*
	17A_43	Zrc	*27660*	*366*	*400220*	*215380*	*2724*		*483*			*506*	*265*	*1139*	*2466*
	17A_65	Zrc	28519		391341	182849	1041	50	158	288	129	692	125	761	1588
	17A_hb1	Hb	29582		388092	179203	2246	45	547	430	1941	368	566	1779	3979
	17A_hb2	Hb	28528		387427	179467	1815	62	465	382	2796	546	386	1563	3356
	17A_hb3	Hb	27300		388699	180215	1478	40	654	582	1639	555	299	1849	3533
	17A_hb4	Hb	28715		388544	180399	1408	65	593	423	2573	504	299	1429	2763
	17A_hb5	Hb	27213	819	388302	179528	1641	42	709	433	2433	523	263	1373	2567
	17A_hb6	Hb	27564		390213	179617	1498	34	384	439	1717	621	335	1101	2423
	17A_hb7	Hb	32125		392403	180358	334	15	155	323	720	588	200	277	573
	17A_hb8	Hb	*30311*	*279*	*400220*	*212920*	*2383*		*591*			*447*	*295*	*1119*	*2441*
	17A_hb9	Hb	*32059*	*428*	*400220*	*213580*	*2383*		*583*			*450*	*267*	*1257*	*2695*
	17A_hb10	Hb	*31494*	*182*	*400220*	*214400*	*2765*		*359*			*438*	*372*	*1256*	*2787*
	17A_bt1	Bt	25570		388246	178542	1390	39	816	417	1546	551	444	1879	3931
	17A_bt3	Bt	29884		388215	178135	1272	98	574	501	4592	228	434	956	2157
	17A_bt4	Bt	27470		387306	178242	1746	73	620	454	3784	357	662	1386	2917
	17A_bt5	Bt	29256	503	387903	179523	1600	141	560	377	3641	448	639	1220	2604
	17A_bt6	Bt	30038	659	391080	181337	804	38	412	305	3107	505	14	404	521
	17A_bt7	Bt	26187		387192	176239	1483	30	623	503	2367	308	582	1484	3085
	17A_bt8	Bt	*28405*	*345*	*400220*	*214420*	*3636*		*840*			*378*	*262*	*712*	*1552*
	17A_bt9	Bt	*27977*	*251*	*400220*	*211850*	*2317*		*1054*			*389*	*328*	*1410*	*2995*
	17A_bt10	Bt	*28930*	*247*	*400220*	*215550*	*1947*		*610*			*382*	*210*	*644*	*1358*
	17A_bt11	Bt	*28999*	*399*	*400220*	*213140*	*2274*		*659*			*362*	*417*	*970*	*2196*
	17A_bt12	Bt	*28726*	*186*	*400220*	*219290*	*1300*		*686*			*359*	*193*	*480*	*1067*
	17A_bt13	Bt	*31169*	*297*	*400220*	*217830*	*44811*		*478*			*362*	*489*	*1042*	*2376*
	17A_kspar1	K-Spar	27101		384994	179702	1905	7	616	397	204	519	273	1954	3156
	17A_kspar2	K-Spar	30989	429	385206	179046	6389	97	520	369	258	668	258	766	1858
	17A_kspar3	K-Spar	28277	567	376551	172911	4828	29	303	422	249	324	594	1328	2992
	17A_kspar4	K-Spar	31288		389823	179764	1212	50	434	351	1060	522	291	953	1953
	17A_kspar5	K-Spar	28819	431	388481	180705	1653	44	543	368	291	653	246	1788	3013
	17A_qtz1	Qtz	32299	395	376136	171682	7172	56	806	397	202	423	307	1833	3358
	17A_qtz2	Qtz	26245		390436	180415	1250	2	409	418	142	234	1605	683	1903
	17A_qtz3	Qtz	30882		391880	180030	890	40	499	387	793	573	143	416	889
	17A_qtz4	Qtz	*29591*	*252*	*400220*	*207140*	*3784*		*946*			*463*	*572*	*2669*	*5437*
	17A_qtz5	Qtz	*28019*	*254*	*400220*	*212140*	*2121*		*879*			*470*	*253*	*1396*	*2744*
	17A_qtz6	Qtz	*29572*	*387*	*400220*	*213420*	*28071*		*706*			*434*	*258*	*800*	*1887*
	17A_qtz7	Qtz	*30997*	*595*	*400220*	*215230*	*2160*		*744*			*443*	*230*	*940*	*1983*
	17A_plag2	Plag	33497		388630	178708	1728	0	338	299	123	528	324	1526	3132
	17A_plag3	Plag	26143		386707	176832	2046	31	564	190		454	407	1467	3006
	17A_plag4	Plag	30964	1056	386959	176177	1916	44	563	500	769	390	267	1100	2491

Table 2 - Ims-4f SIMS zircon REE concentrations (ppm)

Zone	Sample	La	Ce	Pr	Nd	Sm	Eu	Gd	Tb	Dy	Ho
1	17_9	0.16	42.2	0.19	3.8	4.1	1.7	15.4	6.0	61	24
1	17_12	0.15	23.9	0.12	1.6	1.8	0.5	5.7	2.2	26	11
1	17_60	0.27	48.0	0.34	4.6	5.5	2.0	25.8	8.5	92	35
1	17_93	0.18	44.7	0.23	2.5	3.5	0.9	16.0	5.9	67	26
1	17_94	0.18	43.9	0.33	3.9	5.1	1.4	19.5	6.2	71	26
1	17_92	0.14	47.4	0.32	3.6	5.8	1.7	24.3	8.1	86	30
1	17_85	0.14	43.3	0.20	5.1	5.5	1.6	23.5	7.4	86	29
1	17_63	0.04	37.2	0.10	1.7	3.4	0.8	15.6	5.6	58	22
1	17_68	0.02	30.8	0.08	0.6	2.3	0.6	10.2	3.8	41	17
2	18_10	0.05	27.3	0.06	1.1	2.4	0.6	9.2	3.5	41	16
2	18_19	0.09	25.9	0.08	1.9	1.7	0.7	7.0	3.2	38	15
2	18_16	0.15	46.1	0.33	5.2	6.5	1.8	27.6	9.6	99	35
2	18_35	2.33	101.7	1.73	17.6	15.0	5.3	48.6	16.4	167	61
2	18_60	0.12	36.0	0.26	3.7	6.0	1.5	20.5	6.5	72	26
2	18_76	0.09	24.1	0.12	0.9	1.4	0.5	6.2	2.4	28	12
2	18_83	0.08	46.5	0.29	4.0	6.2	1.2	25.4	7.7	82	30
2	18_7	0.08	35.4	0.12	1.6	3.1	0.9	14.5	5.1	56	21
2	18_22	0.04	41.4	0.08	1.7	2.3	0.9	9.6	3.9	52	20
2	18_21	0.14	29.2	0.10	0.7	1.2	0.5	7.1	2.3	32	13
3	21_48	0.18	63.2	0.40	3.8	3.7	0.9	16.3	5.8	76	30
3	21_60	0.25	41.3	0.34	2.8	2.3	0.8	8.9	3.6	40	16
3	21_73	0.01	27.0	0.07	0.8	1.5	0.7	7.5	3.3	37	14
3	21_78	0.89	35.5	0.61	4.7	3.2	0.9	9.5	4.0	44	18
3	21_92	0.09	20.6	0.07	0.6	0.9	0.3	5.2	2.1	33	15
3	21_69	0.07	62.5	0.12	2.0	3.4	1.0	15.4	5.8	77	31
3	21_37	0.48	37.0	0.31	2.9	2.7	1.0	10.5	3.5	45	18
3	21_38	0.37	39.3	0.26	4.2	5.6	2.4	23.1	8.0	83	31
3	21_46	0.21	49.0	0.15	1.5	1.8	0.8	11.9	4.4	50	19
4	22_7	0.61	24.6	0.57	5.3	4.0	1.6	14.3	5.7	59	22
4	22_62	0.15	15.8	0.10	0.9	1.2	0.4	8.0	3.5	44	19
4	22_92	0.30	13.8	0.19	1.4	0.9	0.5	3.3	1.9	28	12

Figure 1
Click here to download high resolution image

Figure. 1

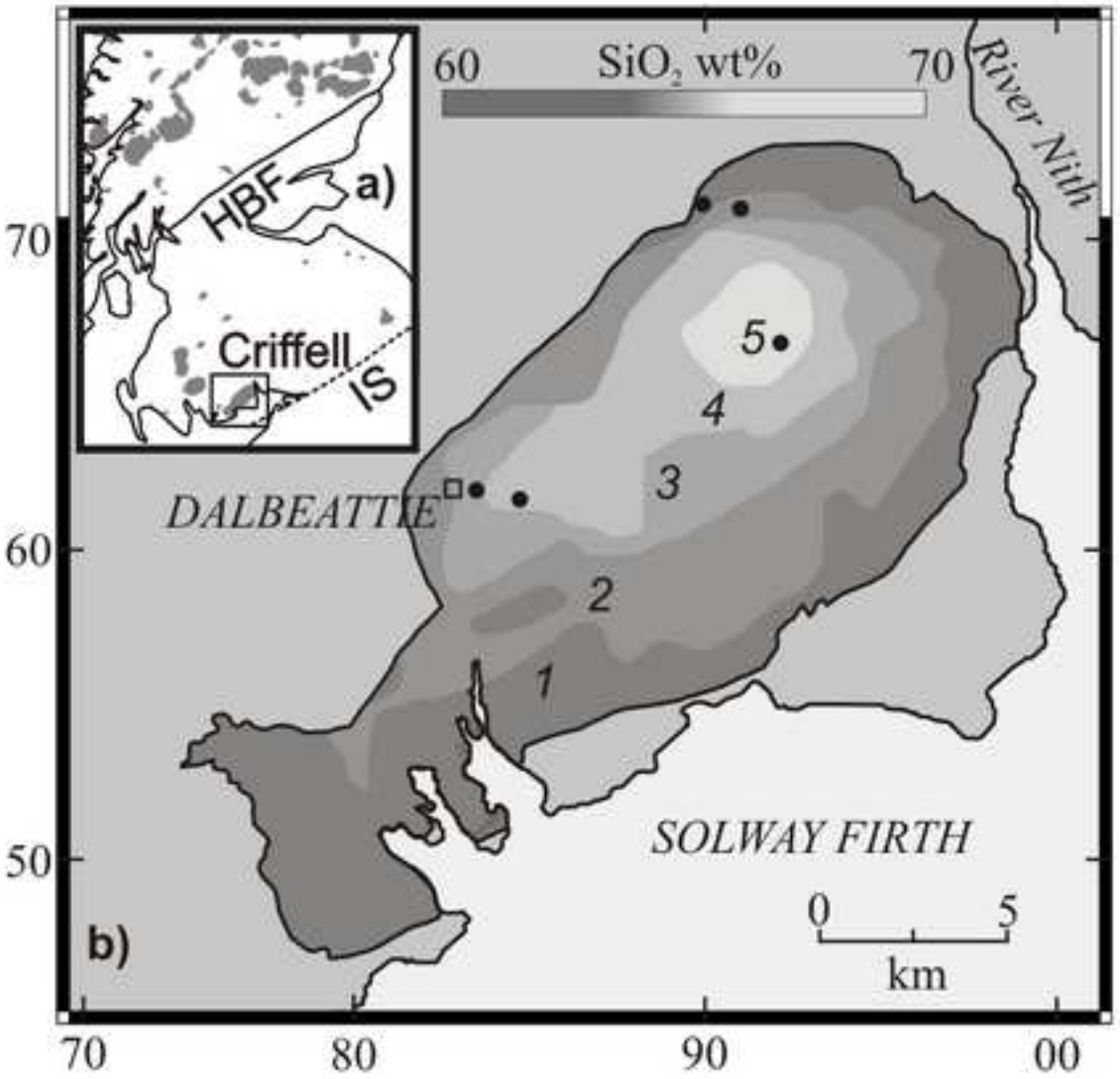

Figure 2

Click here to download high resolution image

Figure 2

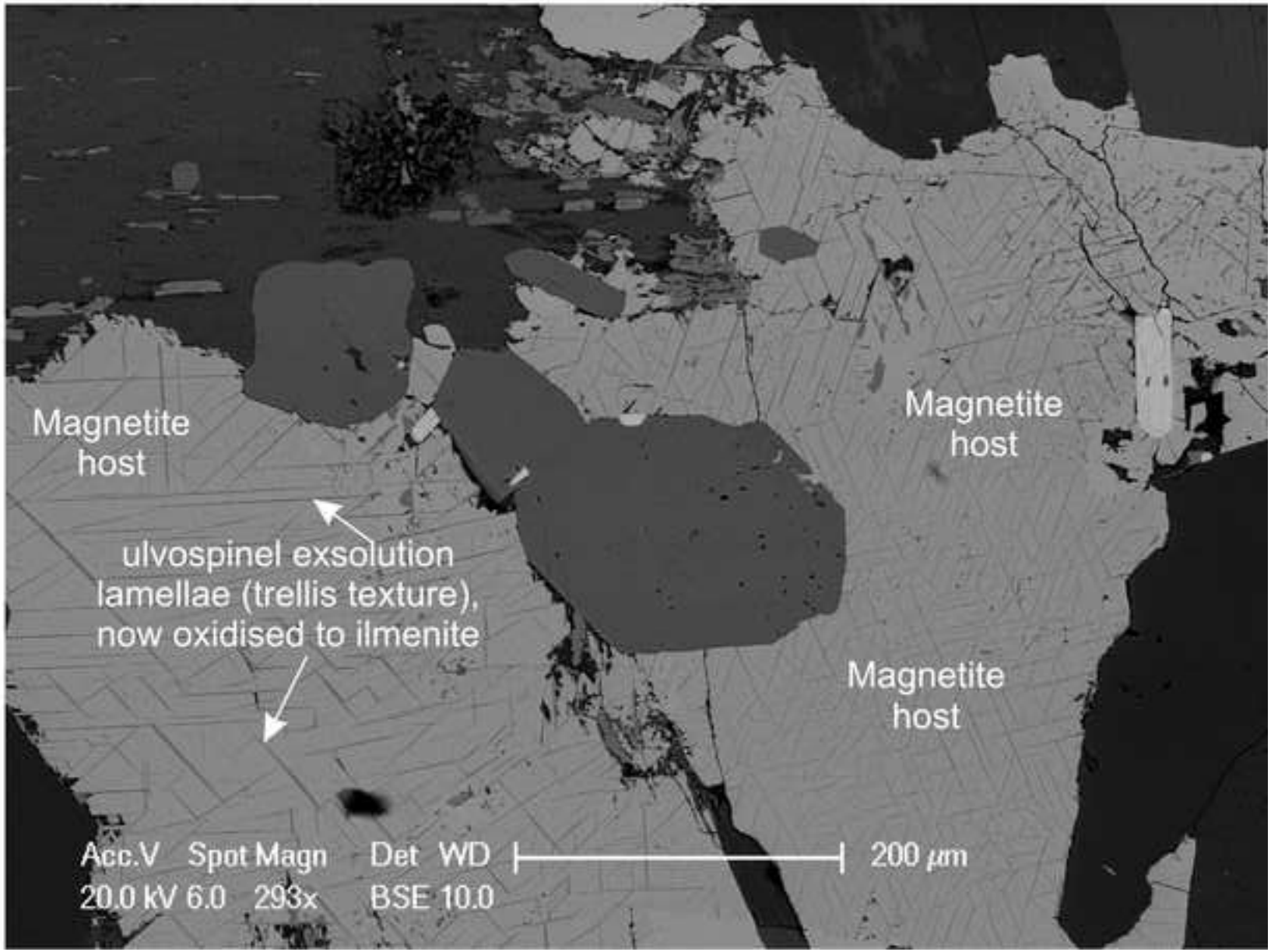

Figure 3

Click here to download high resolution image

Figure 3

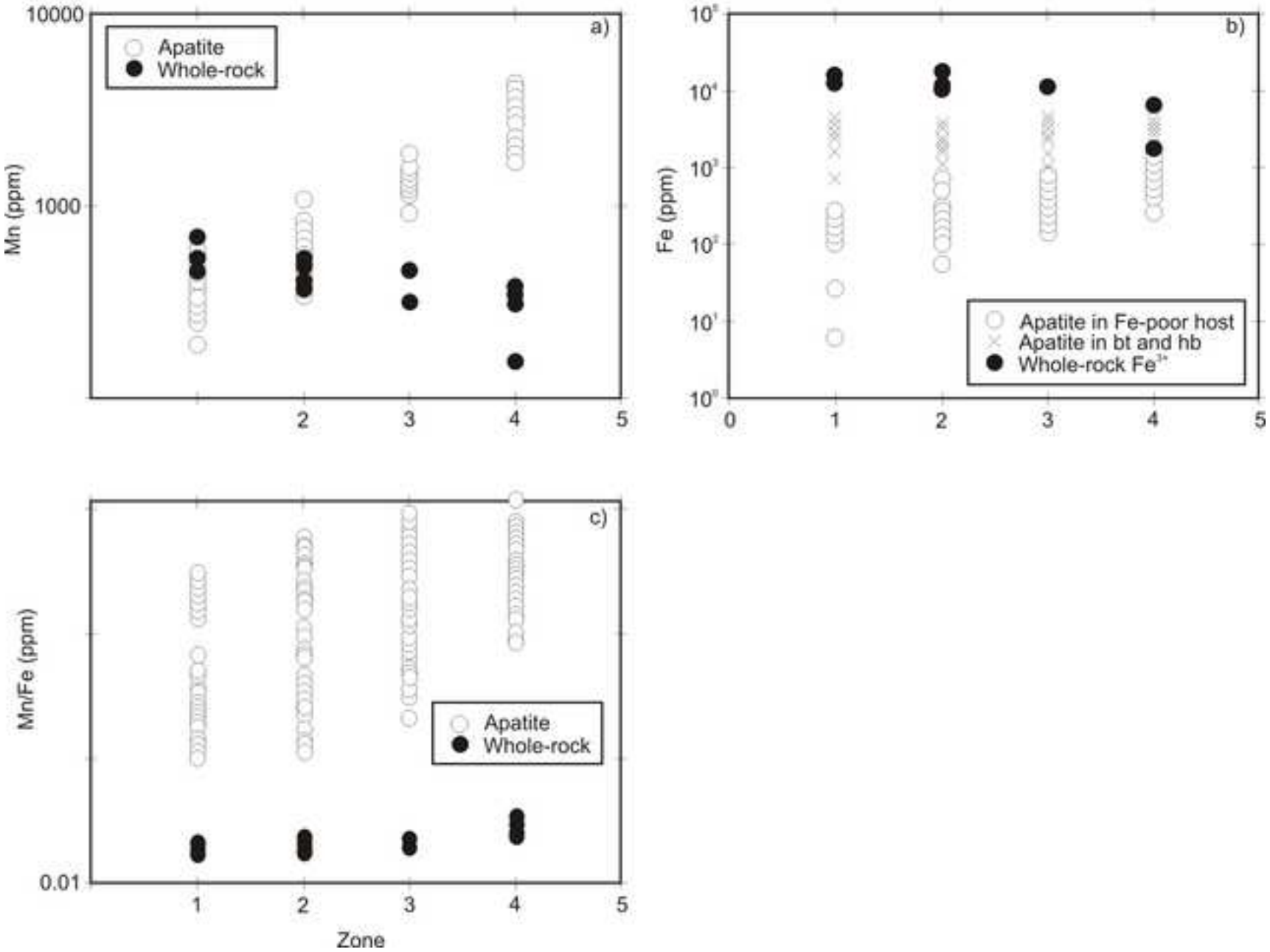

Figure 4
Click here to download high resolution image

Figure 4

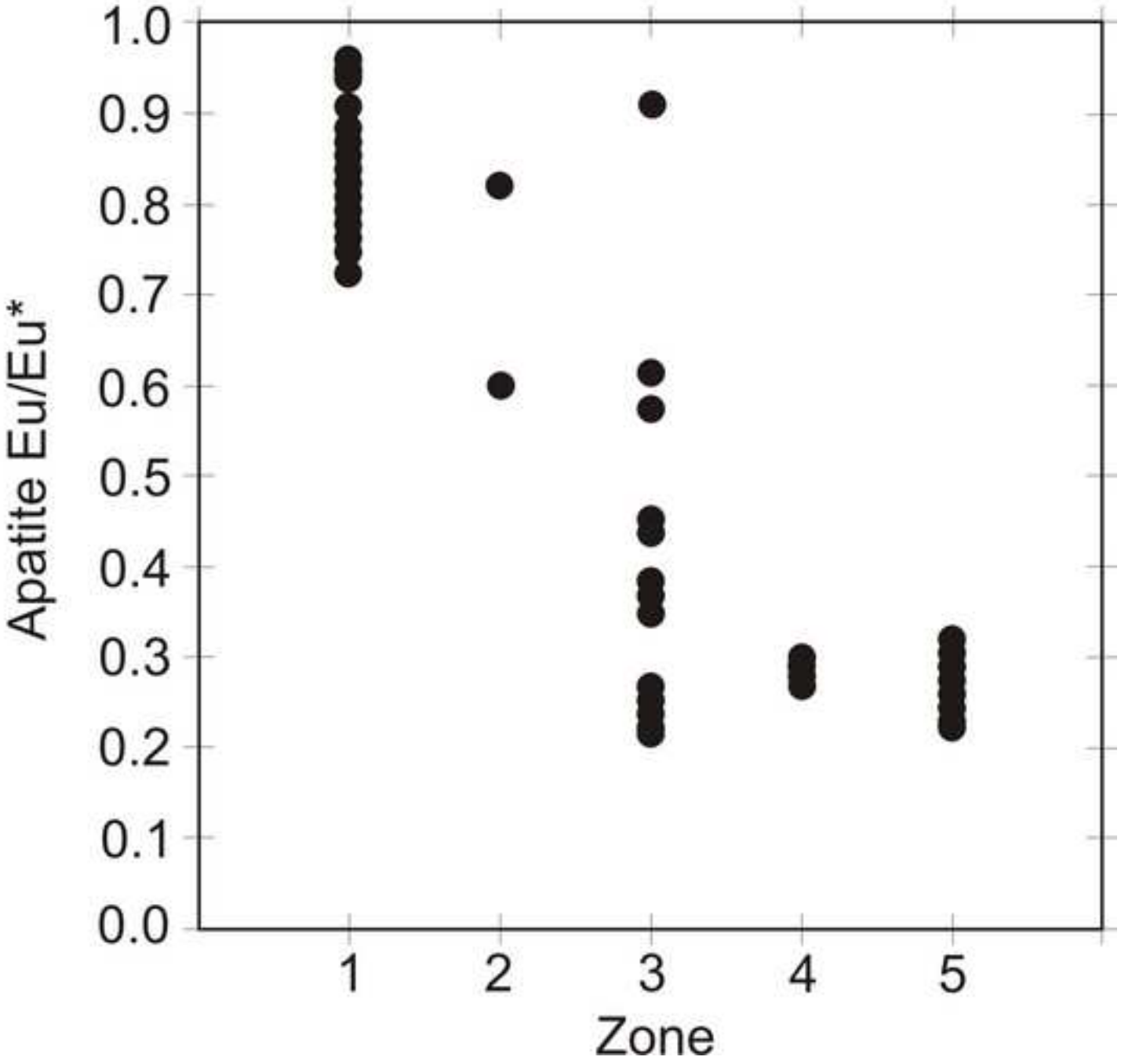

Figure 5
Click here to download high resolution image

Figure 5

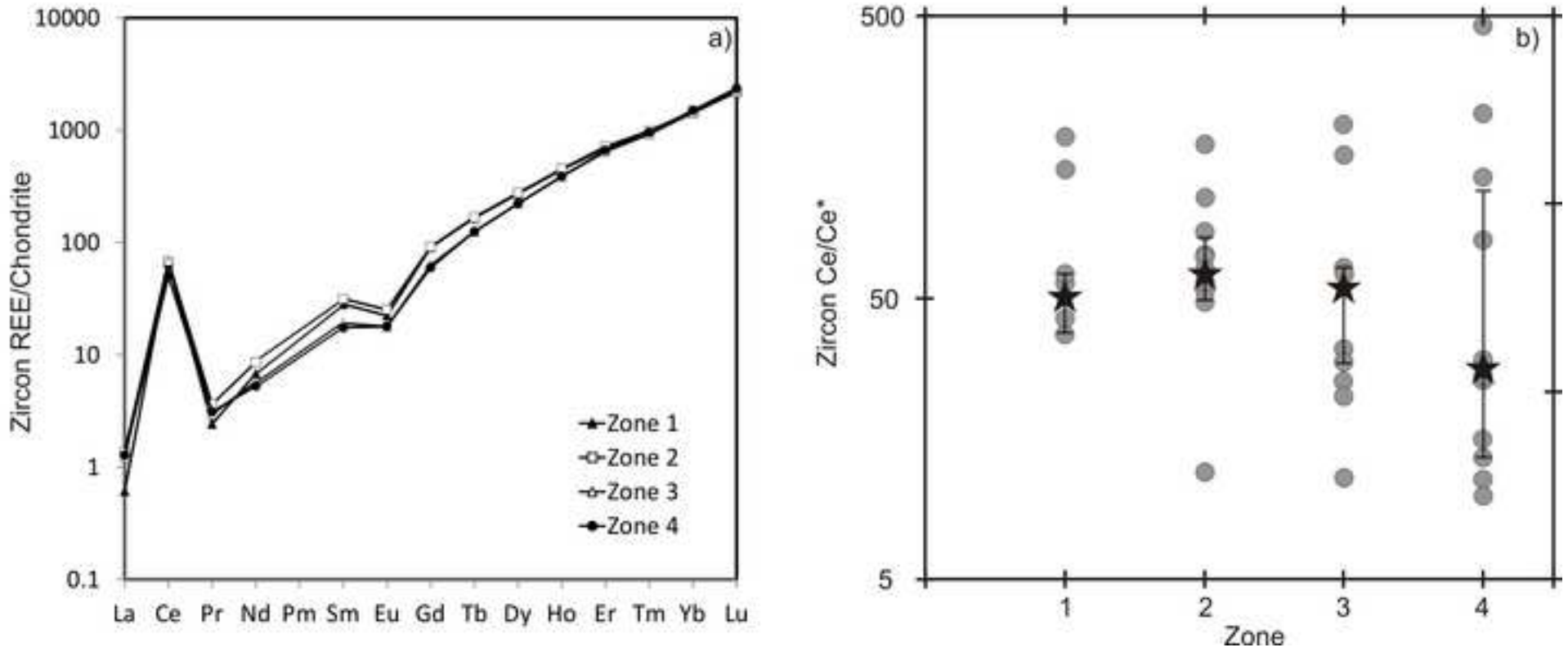

Figure 6

Click here to download high resolution image

Figure 6

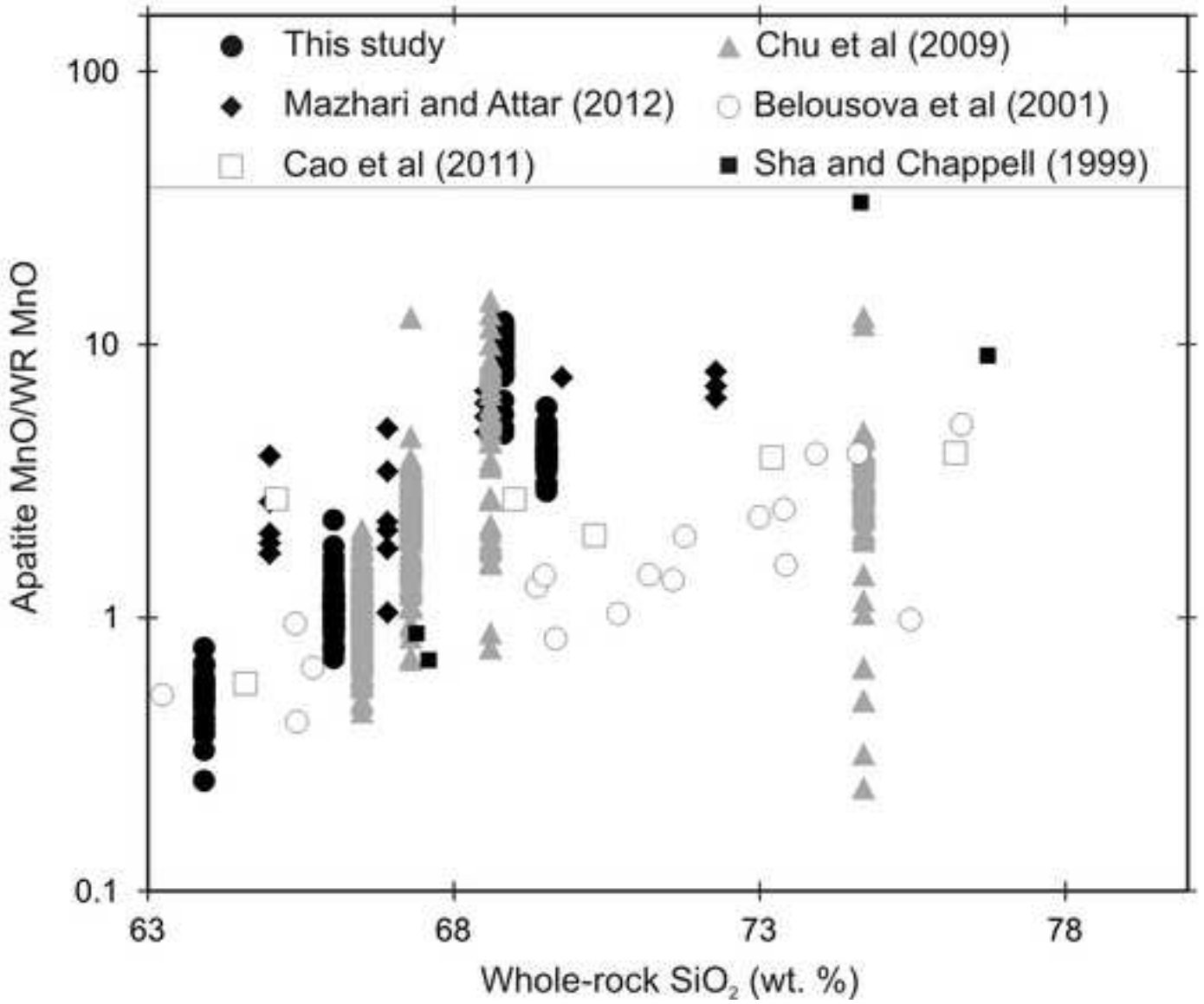

Figure 7

Click here to download high resolution image

Figure 7

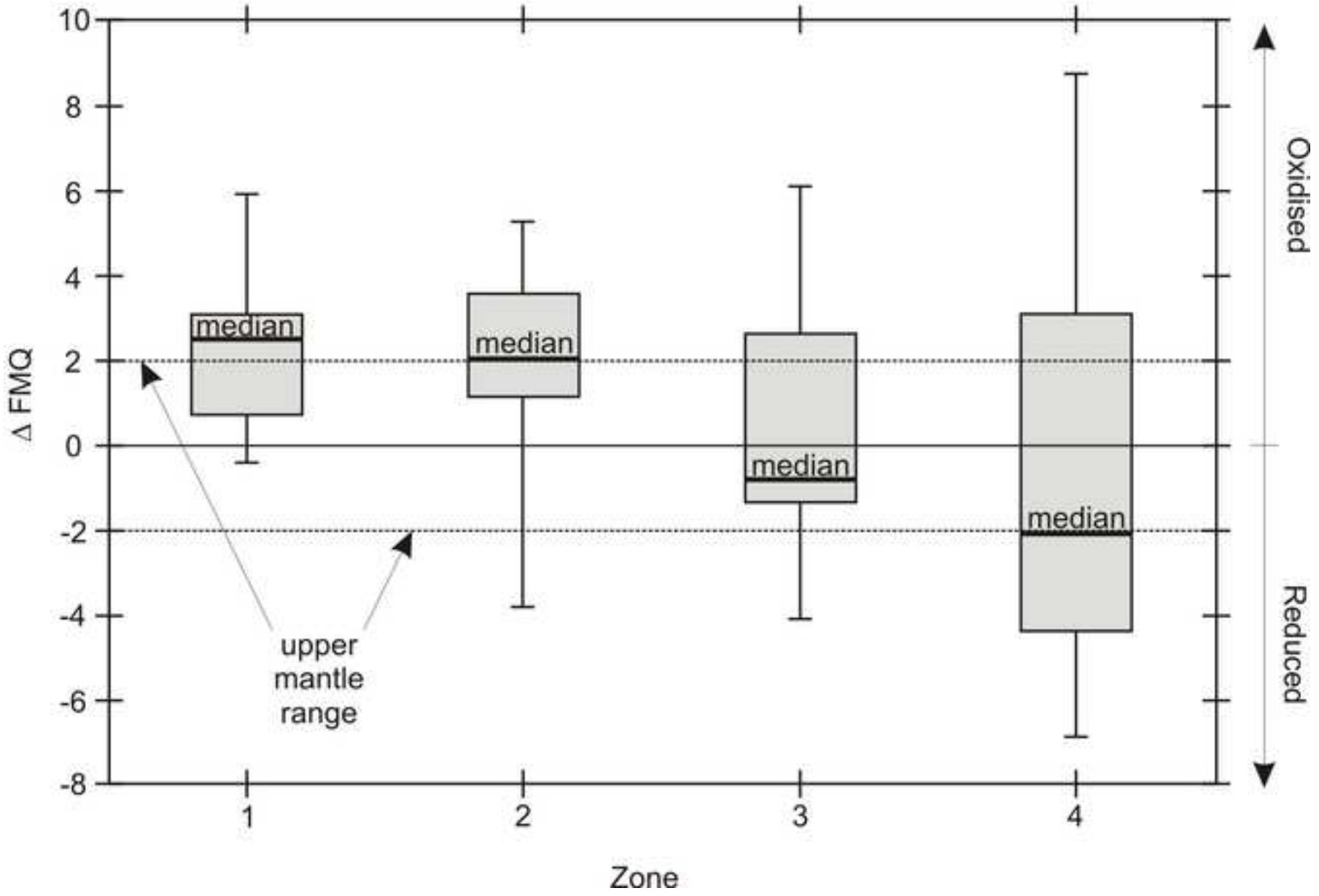

Figure 8

Click here to download high resolution image

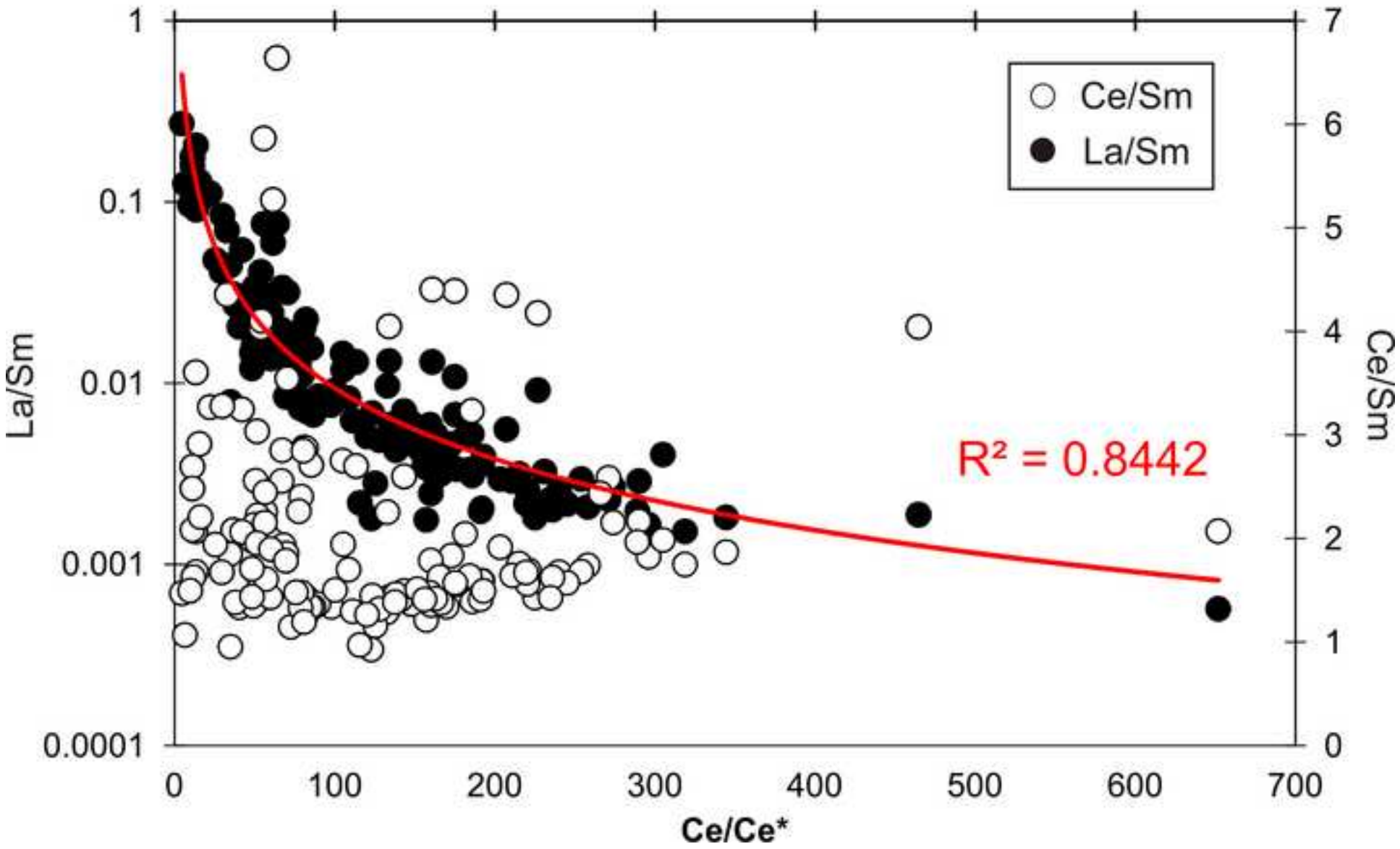

Figure 9

Click here to download high resolution image

Figure 9

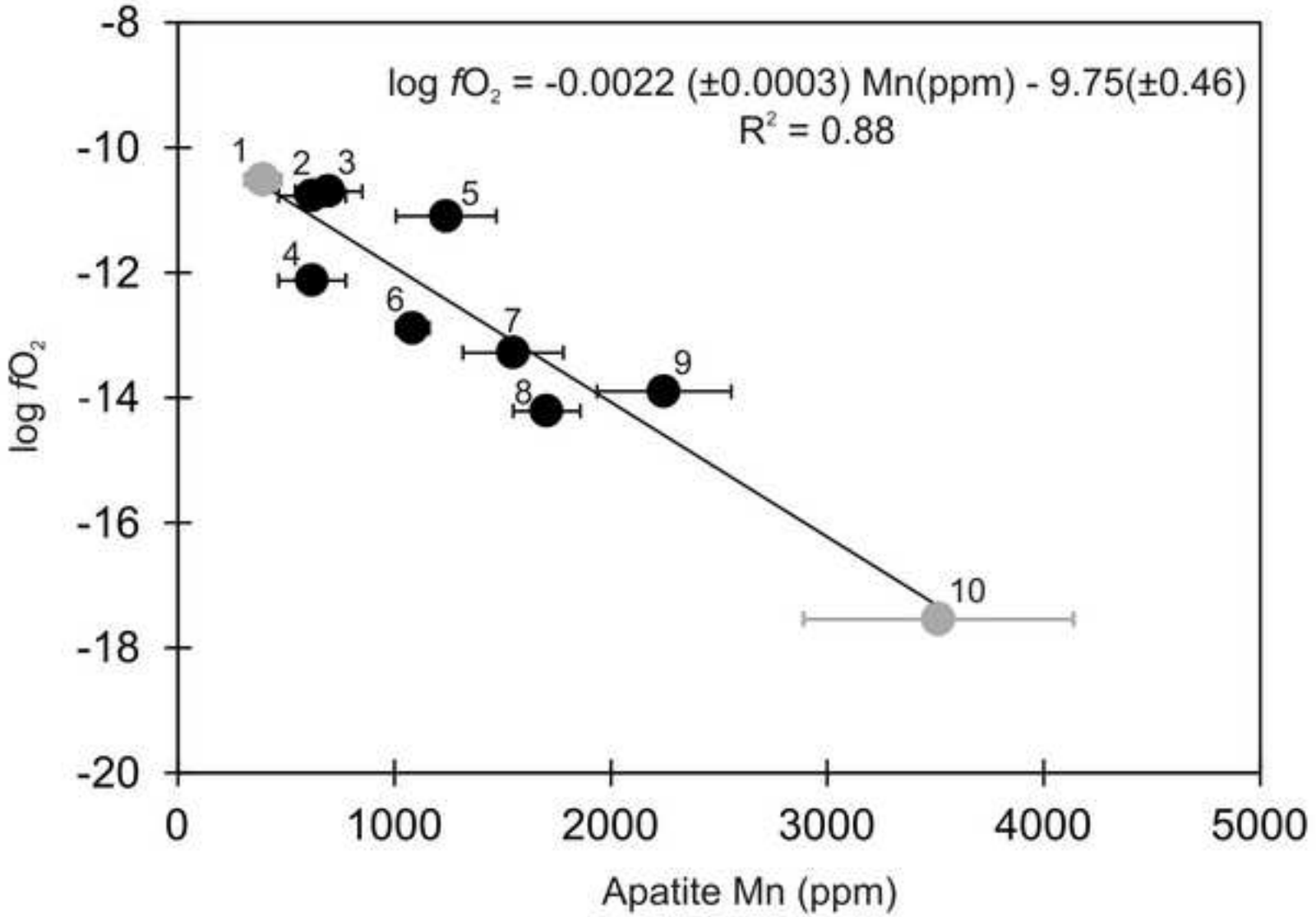

Supplementary Material 1

Click here to download Electronic Annex: Supplementary _1.xls

Supplementary Material 2

Click here to download Electronic Annex: Supplementary_2..xls

Supplementary Material 3

Click here to download Electronic Annex: Supplementary_3.xls

Supplementary Material 4

Click here to download Electronic Annex: Supplementary _4...xlsx

Supplementary Material 5

Click here to download Electronic Annex: Supplementary _5...xlsx